ELSEVIER

Chemical Geology 215 (2005) 127–153

CHEMICAL GEOLOGY
INCLUDING
ISOTOPE GEOSCIENCE

www.elsevier.com/locate/chemgeo

Evaluation of argon ages and integrity of fluid-inclusion compositions: stepwise noble gas heating experiments on 1.87 Ga alunite from Tapajós Province, Brazil

G.P. Landis[a,*], L.W. Snee[a], C. Juliani[b]

[a]*U.S. Geological Survey, MS 963, P.O. Box 25046, Denver Federal Center, Denver, CO 80225, USA*
[b]*Instituto de Geosciências-Universidade de São Paulo, Rua do Lago, 562, Cidade Universitária, CEP: 05508-900, São Paulo-SP, Brazil*

Accepted 1 June 2004

Abstract

Quantitative analyses are reported for active (N_2, CH_4, CO, CO_2, H_2, O_2, HF, HCl, H_2S, SO_2) and noble (He, Ar, Ne) gases released by crushing and step heating of magmatic-hydrothermal alunite from the Tapajós gold province in Brazil. This is the oldest known alunite ($^{40}Ar/^{39}Ar$ age of 1.87 Ga), and because it has undergone minimal postdepositional thermal or tectonic strain, it is excellent material to test the retention of gas species in fluid inclusions and within the crystal structure over geological time. The gas compositions of a single sample, in combination with Ar age-spectrum data derived from stepwise heating of 10 related samples, have been used to constrain the limits of modification of primary gas compositions in fluid inclusions and the possible extent of the loss of radiogenic Ar. The observed variations in the isotopic compositions of He, Ne, and Ar released by stepwise heating have been used to identify the residence sites and determine the diffusion coefficients of the gases in the mineral. The data suggest that the only modification to primary gas compositions after entrapment in fluid inclusions and formation of the mineral is due to radiogenic and nucleogenic processes which affect the noble gas isotopic compositions.

Three gas retention sites are recognized in alunite: (1) primary fluid inclusions, (2) crystal structure OH sites, and (3) crystal structure sulfate sites. Alunite undergoes OH loss at <500 °C, and K-SO_4 structural decomposition occurs at >600 °C. Fluid inclusions generally are ≤1 μm in diameter and have variable but high vapor/liquid ratios. The gases in inclusion fluids are quantitatively released in vacuo by heating at 200 °C for ~1 h. In the inclusion fluids, H_2O is 32 mol% of total gas, H_2S/SO_2 ranges from approximately 4 to 2, and N_2/Ar from 0.3 to 96.3. The presence of large amounts of H_2 and CO indicates disequilibrium among the gas species in the fluids. Helium abundance is 214 ppm. Helium from fluid inclusions (R/Ra=19.5) makes up about 4% of the total helium, whereas He (R/Ra=0.2–2.0) from the crystal structure makes up about 65% of the total. Argon from fluid inclusions has $^{40}Ar/^{36}Ar$ = 584–629 and that from crystal structure sites is $>9.6\times10^4$. Most gases are released from fluid inclusions at 200 °C, whereas most Ar (≥95%) is released between 525 and 725 °C.

* Corresponding author. Tel.: +1 303 236 5406; fax: +1 303 236 6030.
E-mail address: g_landis@usgs.gov (G.P. Landis).

0009-2541/$ - see front matter. Published by Elsevier B.V.
doi:10.1016/j.chemgeo.2004.06.036

Argon released from fluid inclusions at 200 °C has $^{38}Ar/^{36}Ar$ = 0.0–0.064. In contrast, Ar released from the matrix of the mineral at high temperature has $^{38}Ar/^{36}Ar$ = 3.6–14.7. This difference suggests that, since the formation of the alunite at 1.87 Ga, traces of Cl in the mineral structure have undergone Cl (n, γ) and ^{41}K (n, α) in situ reactions with neutrons derived from U–Th. The amount of ^{36}Ar production from Cl nucleogenic reactions used in correcting for atmospheric ^{40}Ar typically increases the calculated age by 1–5 m.y., which is generally an insignificant component of the determined Ar age. Decay of U–Th over this time contributes ^{4}He (α) buildup in the crystal structure K-SO_4 sites. Atmospheric corrected excess $^{21}Ne/^{22}Ne$=0.028–0.409 indicates that nucleogenic Ne was also produced via (α, n) reactions in matrix sites.

Diffusion coefficients and activation energies for the diffusion of Ar and He, as determined using Arrhenius plots, indicate two distinct groups definable by their differences in activation energies. Argon log D_o=2.45 and 15.33, with activation energies of 225 and 465 kJ mol^{-1}, respectively; the diffusion of He in alunite is quantified with log D_o=−4.33 and E=106.8 kJ mol^{-1}. Model calculations of simplistic 1/e-folding times and diffusion distance–time curves indicate that He should remain in alunite for millions of years at ≤100 °C, whereas at <200–220 °C, the alunite will retain Ar almost indefinitely. The data demonstrate why alunite is suitable for Ar geochronological applications and also show that, unless the alunite is subjected to metamorphic deformation, the inclusion fluids should retain their primary compositions.
Published by Elsevier B.V.

Keywords: Argon ages; Fluid inclusion compositions; Noble gases; Alunite; Tapajós; Brazil

1. Introduction

The discovery of coarse-grained samples of 1.87 Ga alunite from the Tapajós gold district in the Brazilian Amazonian craton (Juliani et al., this volume) offers an opportunity to evaluate how well the composition of primary fluid inclusions and matrix gas are preserved in the mineral over geological time. Alunite [$KAl_3(SO_4)_2(OH)_6$] forms in hydrothermal and supergene environments; magmatic-hydrothermal alunite, as occurs in the Tapajós district, is the common type in high-sulfidation mineral deposits. Stable isotope analyses of alunite have proven useful in studies of the formation of mineral deposits (Rye et al., 1992), and the mineral can be dated by K-Ar and $^{40}Ar/^{39}Ar$ geochronological methods. Furthermore, the compositions of gases in inclusion fluids seem to provide important constraints on the magmatic-hydrothermal processes of alunite formation (Landis and Rye, this volume). However, no studies of gas diffusion have been done to document the ability of the mineral to retain primary Ar-gas compositions in its matrix or to retain primary fluid compositions in its fluid inclusions. In this study, the noble gas and active gas contents of fluid extracted from inclusions and mineral matrix of alunite from the 1.87 Ga Tapajós gold district were analyzed. The active gases referred to are N_2, CH_4, CO, CO_2, H_2, O_2, HF, HCl, H_2S, and SO_2, and the noble gases are He, Ne, and Ar.

Analyses of the gases were conducted on fluids released in vacuo by crushing and subsequent stepwise heating of a single sample of nonirradiated coarse-grained alunite. In conjunction, experiments on the thermal release of Ar were completed on 10 related samples that were irradiated and measured for their Ar ages. The data from both sets of experiments are used to recognize three discrete sites of gas retention and to model diffusion properties of He and Ar in alunite. Most of the gases are shown to have been derived both from fluid inclusions and from two sites within the mineral structure. The data are used to test the hypothesis that the primary gas composition of fluids may be retained in fluid inclusions of unmetamorphosed alunite for at least 1.87 Ga. If the fluid inclusions in alunite generally retain their gas compositions over such long periods of geological time, then it is likely that the composition of fluids in inclusions from much younger alunite will be preserved. Consequently, the data for fluid inclusion gas can be used to characterize the compositions of the parental fluids that were trapped in alunite at the time of its deposition (Landis and Rye, this volume).

It has been shown that alunite can be used for K-Ar and $^{40}Ar/^{39}Ar$ geochronology (Ashley and Silberman, 1976; Bird et al., 1990; Vasconcelos et al., 1994; Dammer, 1995; Vasconcelos, 1999). The results of this study have confirmed that alunite from the 1.87 Ga Tapajós deposit (Juliani et al., this volume) has

remarkable Ar retention, and it is shown that the reason is that the diffusion coefficients of Ar in coarse-grained alunite are so low.

2. Sample description and gas analysis

A nonirradiated split of Tapajós alunite sample X1-16/18 was used to determine the noble and active gas compositions in alunite-hosted fluid inclusions and its mineral structure (matrix) sites. In addition, this and nine other alunite samples were irradiated and analyzed for Ar geochronology. The detailed Ar geochronological data from these 10 samples are used in Juliani et al. (this volume) to constrain the timing of gold mineralization in the Tapajós high-sulfidation deposit. Selected parts of the Ar geochronological data are combined below with the data for noble gas from sample X1-16/18 to quantify diffusion coefficients and activation energies of gases in alunite.

2.1. Noble and active gases and fluid inclusions

A sample of X1-16/18, consisting of several ethanol-washed and weighed pieces of alunite (total 6.96 g), each 0.5 to 1.0 cm on a side, was analyzed in several steps. The sample was crushed off-line in vacuo and returned to the manifold. The fluid was extracted, and its gases were analyzed. The alunite was then heated in the same crush tube to 200 °C for 60 min twice, and each time, the thermally released gases were analyzed. Active gas compositions were analyzed by quadrupole mass spectrometry using methods similar to those described by Landis and Hofstra (1991), and noble gas isotopic and elemental compositions were determined by both noble gas (MAP215-50) and quadrupole (Pfeiffer Prisma) mass spectrometry. Larger remaining pieces (0.1 to 1.0 mm) then were taken from the crush tube and placed into an on-line stainless steel tube resistance furnace, evacuated to ultrahigh vacuum, heated to 200 °C for 60 min, and for the third time, the released gas was analyzed. The second 200 °C thermal extraction yielded <2% of the total gas released at that temperature, indicating that nearly all fluid inclusion gases were released during crushing and the first thermal extraction at 200 °C. A third thermal extraction at 200 °C did not yield sufficient gas for analysis by quadrupole mass spectrometry. Gases released during subsequent heating at 100 °C increments to 700 °C were analyzed only for He, Ne, and Ar isotopes on the MAP215-50 mass spectrometer.

2.2. Thermal release of Ar

Ten additional alunite samples were irradiated, and their Ar isotopes were analyzed. The 10 included a split of X1-16/18, which was studied in detail for other noble and active gases. The stepwise heating experiments employed in age-spectrum determinations (Juliani et al., this volume) yielded temperature release profiles useful in modeling the diffusion of Ar in alunite. Selected parts of the data for Ar release during stepwise heating in standard $^{40}Ar/^{39}Ar$ age determinations are used here to evaluate the diffusion parameters for Ar and the effects of nucleogenic production of Ar isotopes; detailed data are presented in Juliani et al. (this volume).

3. Results

3.1. Description of alunite and fluid inclusions

3.1.1. Geological setting

Sample X1-16/18 is from the upper levels of a volcanic ring complex that hosts a 1.87-Ga gold occurrence in the Tapajós province of the Brazilian Amazon. The nine additional alunite samples used for Ar geochronology are from near-surface exposures and drill cores. Near-surface samples were not subjected to cosmogenic production of nuclides; all were collected many meters below the original surface and were exposed only by recent mining operations.

Tapajós alunite is identified by Juliani et al. (this volume) as magmatic-hydrothermal, according to the criteria of Rye et al. (1992). The alunite formed during high-sulfidation mineralization that was genetically linked to volcanic magmatic activity along the 1.87-Ga continental margin of the Amazonian craton. The five varieties of alunite (A_1–A_5) recognized at Tapajós are described by Juliani et al. (this volume). Alunite sample X1-16/18 is from stage A_5, which is a late-stage, rose-colored, fine-grained, randomly oriented alunite that crosscut and replaced the branching crystals of stage A_4. Geological evidence and the Ar

geochronology (Juliani et al., this volume) indicate that the alunite has been protected since formation by burial in a shallow graben and has been subjected only to brief and episodic low-temperature thermal (dike intrusion) activity and localized shearing events that occurred shortly after alunite formation. Since early postdeposition, the alunite has remained thermally undisturbed. The host rocks exhibit no evidence of later metamorphism, and no evidence is known for deep burial or sustained high geothermal gradients. More extensive descriptive details, paragenetic relations, and the geologic framework of Tapajós alunite stages are well documented in Juliani et al. (this volume).

3.1.2. Mineralogy

As a hydrated potassium–aluminum sulfate [$KAl_3(SO_4)_2(OH)_6$], alunite is comprised of crystal structure intervals perpendicular to the *c* axis that alternate between tetrahedrally coordinated S atoms bonded with O and K and octahedrally coordinated Al bonded with O and OH. Important stoichiometric substitutions of Na for K, Fe for Al, P for S, and F and Cl for OH are possible (Brophy, 1960; Brophy et al., 1962). Alunite loses its structural OH at ≤500 °C and undergoes crystal disintegration by loss of SO_3 at >600 °C (Slansky, 1973; Fielding and Sclar, 1980; Fielding, 1981). These crystallographic effects and the loss of stoichiometric components with experimental thermal extraction facilitate the release of gas from alunite.

Alunite sample X1-16/18 is pure and massive, consisting of a polycrystalline aggregate of plates that are 5–20 μm thick and commonly only 20–80 μm across. Larger contiguous crystal domains 0.2–3.0 mm across are also common. The size of the crystal domains of other alunite samples analyzed in this study range from that of X1-16/18 to a few micrometers. One sample, FV3-1/12, consists of thin (a few micrometers) plates formed by shear deformation.

3.1.3. Alunite chemistry

Electron microprobe compositions, which are the average of 10–12 points per sample, are given for X1-16/18 in Table 1. The sum of the different elements averages 84.86 wt.%, with the remainder taken to be OH. Each alunite is grouped as having low or high diffusion activation energy in accordance with its measured diffusion parameters. The compositions of Tapajós alunite are similar to those of other magmatic-hydrothermal alunite samples (Deyell et al., this volume; Juliani et al., this volume). Although the studied samples are mainly alunite in composition, a solid solution extends to natroalunite (Na substitution for K) as represented by several of the samples. For convenience, the series is simply referred to as alunite. The two groupings according

Table 1
Average electron microprobe compositions of alunite

Wt.%	Low activation energy			High activation energy		
	FV3-1/16[1]	X1-16/18	X1-16G	FV3-1/25	FV3-1/11	X1-16F
n	10	10	10	10	11	12
K_2O	5.11	6.51	8.55	9.53	8.05	9.50
Na_2O	3.71	2.74	1.34	0.76	1.24	0.75
CaO	0.20	n.d.	0.27	n.d.	n.d.	n.d.
BaO	n.d.	0.34	0.76	0.50	0.37	0.46
Al_2O_3	37.29	37.05	36.71	36.83	37.18	36.40
SO_3	37.84	37.71	36.94	36.66	36.79	36.64
P_2O_5	0.28	n.d.	0.45	0.50	0.45	0.34
F	n.d.	0.96	0.81	1.00	n.d.	n.d.
Cl	n.d.	n.d.	0.07	n.d.	0.05	n.d.
Total	84.64	85.46	85.01	85.46	84.46	84.15
Temperature [°C]		250	130	420	260	420
$\delta^{34}S$		26.7	38.2	14.0	15.8	14.3

n—number of analyses; n.d.—below detection limit; Fe, U, Th, Cu, Pb, Ag not detectable. Sulfur-isotope data and calculated temperature from alunite–pyrite sulfur isotopic fractionation are from Juliani et al. (this volume). Low and high activation energy refer to diffusion parameters determined for these alunite samples (Tables 6a,6b).

to activation energy also exhibit different $\delta^{34}S_{alunite}$ and $\Delta^{34}S_{(alunite\text{-}pyrite)}$ calculated temperatures (Juliani et al., this volume). In comparison, the alunite samples with high activation energy are enriched in K (K_2O/Na_2O=6.48 vs. 1.70 molar), and the samples with low activation energy show slightly greater amounts of P-for-S substitution. Because radiogenic Ar and He in alunite are held within the K-linked sulfate tetrahedra, these crystal structure differences may be important in gas retention.

3.1.4. Fluid inclusions

Generally, fluid inclusions are ≤1 μm in diameter, have high gas/liquid ratios, and are too small for detailed temperature-salinity-clathrate studies (Roedder, 1984). The photomicrograph images in Fig. 1 show rare 1–2-μm gas-rich inclusions. Most inclusions are 0.01 to 0.2 μm and appear to be gas rich. The distance from the surface of the inclusions to the crystal domain boundaries is the limiting dimension to diffusion of gas out of the inclusions because loss or exchange to the surrounding environment is likely to be rapid once the gas reaches the edge of the domain crystallite.

Fluid inclusions in Tapajós alunite are typical of those observed in hydrothermal alunite from other localities (Cunningham et al., 1984; Landis and Rye, this volume). The alunite in this study contains three varieties of primary fluid inclusions as defined by their relation to crystallographic features. All observed inclusions have similar gas/liquid ratios and generally are gas dominant. Type 1 fluid inclusions are elongate parallel to the alunite *c* axis and commonly are concentrated at micrometer to submicrometer crystal domain boundaries. These boundaries are recognized by a change in optical properties, with epitaxial growth of alunite in a subtly different crystal orientation. Type 2 inclusions occur in trains parallel to the surfaces of mineral deposition (growth bands). These inclusion trains are aligned perpendicular to the principal deposition direction, which is outward from the base of the crystal. Type 3 inclusions are randomly dispersed, somewhat elongate, and have no preferred orientation or location, but all are within the interiors of optically definable crystal domains. Planes of secondary fluid inclusions are rare and occur as wispy trails of dark inclusions and clouded regions generally contained within the boundaries of crystallite domains. Translucent daughter minerals are absent from the gas-rich inclusions and are impossible to recognize with certainty in rare, small liquid-rich inclusions. A notable exception is primary hematite, which is common both as solid inclusions and as nucleation centers for growth of fluid inclusions. The small size and large number of fluid inclusions in alunite certainly favor preservation of trapped fluids. The submicrometer size of the inclusions also increases the likelihood that gases were trapped out of equilibrium with the parental fluid across large chemical gradients at the depositional interface (cf. Landis and Rye, this volume).

3.2. Data for crush-released and thermally released active gas

The results of active gas analyses for crush and 200 °C thermally released fluids are given in Tables 2a,2b. Approximately 98 mol% of the total fluid in the alunite sample was obtained by the crush release and the first of the 200 °C thermal extractions. The second 200 °C extraction released <2 mol% of the total fluid, and a subsequent third extraction at 200 °C did not yield enough fluid (<0.02 mol%) for quadrupole spectrometric analysis of its gas content. In general, the gas composition of X1-16/18 alunite is similar to that of fluids in other magmatic-hydrothermal alunite at other deposits, as discussed by Landis and Rye (this volume).

3.3. Discussion of data for active gases

It is thought that the initial crushing of alunite at room temperature releases the more easily accessed fluids present in larger primary inclusions, in secondary inclusions occurring in healed fractures, and in voids along crystal boundaries. As established in previous studies of fluid inclusions hosted in other minerals (Landis and Hofstra, 1991), this assumption seems to be reasonable for alunite (cf. Landis and Rye, this volume). It is likely that during the thermal extraction of fluids at 200 °C, very small vapor-rich inclusions in the interior of crystal domains open either by thermal decrepitation or by thermal distortion of the crystal, with attendant diffusion of gas from the inclusion sites. Heating to much higher temperatures is required to release noble gas from the

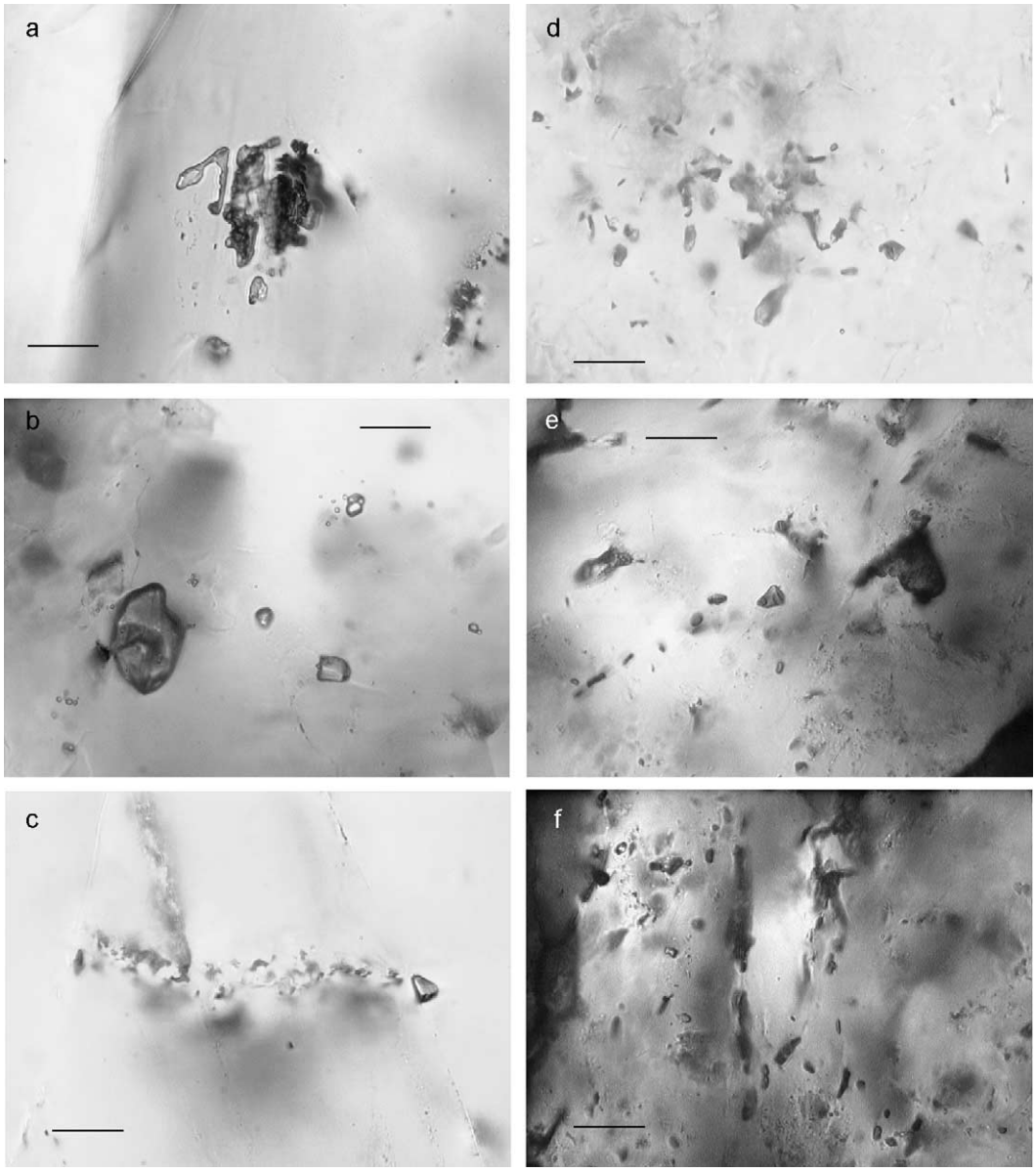

Fig. 1. Photomicrographs of alunite-hosted fluid inclusions. Images (a–c) are of fluid inclusions in the alunite that has the higher He diffusion coefficients, and images (d–f) are of fluid inclusions in the alunite that has the lower He diffusion coefficients. The scale bar in images (a–f) represents 1 μm. (a) Alunite X1-16/18 showing a large gas-rich Type 1 fluid inclusion associated with primary hematite crystals that possibly caused the defect nucleation of a fluid inclusion. (b) Alunite FV3-1/16 showing unusually large hematite-stained gas inclusions of Type 2, with <0.1 μm inclusions visible. (c) Sample X1-16/18 showing gas-rich Type 1 and Type 2 fluid inclusions with no visible meniscus. Type 1 has vertical interdomain boundaries, and Type 2 has horizontal growth bands. (d) Alunite FV3-1/11 showing Type 3 randomly distributed micrometer to submicrometer gas-rich fluid inclusions. (e and f) Sample X1-16F showing larger Type 1 fluid inclusions in alunite with abundant primary hematite. A liquid meniscus is present in the 0.3-μm inclusion centered in 1*e*. Secondary fluid inclusion planes are not evident in any of these images.

Table 2a
Crush release and thermal release gas compositions[a]

Release	Ar [%]	N_2 [%]	H_2O [%]	CH_4 [%]	CO [%]	CO_2 [%]	H_2 [%]
Crush (22 °C)	0.302	29.039	0.859	0.414	67.708	0.155	1.513
(1) 200 °C–60 min	31.491	10.617	10.411	1.251	0.000	38.873	7.263
(2) 200 °C–60 min	0.132	3.733	58.433	3.887	0.515	22.770	10.443
Total mol%	1.021	28.115	2.211	0.501	64.821	1.496	1.822
Total thermal	17.109	7.460	32.435	2.460	0.236	31.488	8.721

Release	O_2 [ppm]	HF [ppm]	HCl [ppm]	H_2S [ppm]	SO_2 [ppm]	He [ppm]	Total moles
Crush (22 °C)	8	30	6	34	8	11	7.1678E-08
(1) 200 °C–60 min	221	76	136	189	110	216	1.7351E-09
(2) 200 °C–60 min	165	0	117	292	94	212	1.4698E-09
Total mol%	16	31	11	42	12	20	7.4883E-08
Total thermal	200	41	128	235	102	214	3.2049E-09

[a] Data are in mol% (or ppm*V*) for the initial crush and for the first and second 200 °C heat extraction of 60 min duration. Total moles of gas released for each extraction are calculated from the Ar calibration (moles/amp), and then a weighted sum of moles for the total of each gas is normalized to calculate total mol% (mole fractions). Total thermal released tabulation is recast to include just the two 200 °C thermal extractions.

sulfate site of the alunite structure (Table 3). The diminished amounts of fluid obtained in the second and third extractions at 200 °C, as well as the noble gas isotope data of the fluid, especially Ar and He, indicate that no fluid was released from the OH or sulfate sites in alunite either by crushing or heating to 200 °C. Therefore, data for the 200 °C thermally released gas in Tables 2a,2b are predominantly from fluid inclusions and may characterize the fluids responsible for the deposition of the host alunite. Landis and Rye (this volume) have demonstrated that gas even in the secondary fluid inclusions is closely linked to deposition of the host alunite.

In this paper, the fluid inclusion gas chemistry is summarized only to demonstrate that exchange with external gas sources or with characteristic gases in the OH and sulfate sites within alunite has not occurred. The geochemical significance of active gases from fluid inclusion sites is discussed in detail in Landis and Rye (this volume). A weighted total of 2.2 mol% H_2O for the fluid (32.4% for weighted total thermally released fluid) indicates that most fluid

Table 2b
Crush release and thermal release gas compositions (water free)[a]

Release	Ar [%]	N_2 [%]	CH_4 [%]	CO [%]	CO_2 [%]	H_2 [%]
Crush (22 °C)	0.304	29.291	0.417	68.295	0.156	1.526
(1) 200 °C–60 min	35.150	11.851	1.396	0.000	43.390	8.107
(2) 200 °C–60 min	0.318	8.980	9.350	1.239	54.778	25.123
Total mol%	1.044	28.751	0.513	66.286	1.530	1.863
Total thermal	25.322	11.041	3.640	0.350	46.603	12.908

Release	O_2 [ppm]	HF [ppm]	HCl [ppm]	H_2S [ppm]	SO_2 [ppm]	He [ppm]
Crush (22 °C)	8	31	6	34	8	12
(1) 200 °C–60 min	247	85	152	209	122	241
(2) 200 °C–60 min	398	0	282	704	226	509
Total mol%	17	31	11	43	12	21
Total thermal	289	61	189	348	152	316

[a] Data are in mol% (or ppm*V*) for the initial crush and for the first and second 200 °C heat extraction of 60 min duration. Total moles of gas released for each extraction are calculated from the Ar calibration (moles/amp), and then a weighted sum of moles for the total of each gas is normalized to calculate total mol% (mole fractions). Total thermal released tabulation is recast to include just the two 200 °C thermal extractions.

Table 3
Noble gas isotope concentrations and ratios, Tapajós X1 16/18 alunite

Temperature [°C]	^{3}He [mol g^{-1}]	^{4}He [mol g^{-1}]	^{20}Ne [mol g^{-1}]	^{21}Ne [mol g^{-1}]	^{22}Ne [mol g^{-1}]	^{36}Ar [mol g^{-1}]	^{38}Ar [mol g^{-1}]	^{40}Ar [mol g^{-1}]
Concentration								
22.4	3.29E-20	1.81E-14	2.53E-14	8.10E-17	2.72E-15	4.98E-15	0	3.01E-12
200	2.33E-18	1.58E-13	6.13E-14	2.08E-16	6.90E-15	1.48E-14	5.03E-18	9.33E-12
308	7.48E-18	2.77E-13	5.87E-15	1.80E-17	6.14E-16	1.81E-14	3.41E-17	1.06E-11
408	3.92E-18	5.29E-13	5.35E-15	1.65E-17	5.53E-16	5.41E-14	3.46E-15	5.50E-11
500	9.08E-19	2.87E-12	6.18E-15	3.20E-17	6.69E-16	5.99E-14	2.14E-13	4.28E-09
600	6.26E-18	2.33E-12	2.80E-14	2.75E-16	3.32E-15	1.67E-13	2.45E-12	1.62E-08
700	1.42E-18	4.35E-12	1.12E-15	4.45E-18	1.33E-16	1.18E-13	4.47E-13	5.45E-09
Total	2.24E-17	1.05E-11	1.33E-13	6.35E-16	1.49E-14	4.36E-13	3.11E-12	2.60E-08

Temperature [°C]	^{3}He/^{4}He (=*R*)	*R*/Ra Ra=1.384E-6)		*R*/Ra (200 °C)	^{20}Ne/ ^{22}Ne	^{21}Ne/ ^{22}Ne	^{21}Ne*	^{22}Ne*	^{21}Ne*/ ^{22}Ne*	^{40}Ar/ ^{36}Ar	^{38}Ar/ ^{36}Ar	^{4}He/ ^{21}Ne*	^{21}Ne*/ ^{40}Ar*	^{4}He/ ^{40}Ar
Ratio														
22.4	1.82E-06	1.31		1=10.60,	9.3045	0.0298	5.53E-18	1.42E-16	0.0390	605	0.0000	3276	1.84E-06	0.0060
200	1.48E-05	10.66	=	2=10.69,	8.8771	0.0301	2.47E-17	6.61E-16	0.0374	629	0.0003	6379	2.65E-06	0.0169
308	2.70E-05	19.50		3=10.44	9.5580	0.0292	4.46E-19	1.62E-17	0.0276	584	0.0019	621,303	4.23E-08	0.0263
408	7.42E-06	5.36			9.6614	0.0298	5.65E-19	8.75E-18	0.0645	1017	0.0639	936,881	1.03E-08	0.0096
500	3.17E-07	0.23			9.2357	0.0479	1.36E-17	3.96E-17	0.3438	71,443	3.5764	210,546	3.18E-09	0.0007
600	2.68E-06	1.94			8.4337	0.0828	1.91E-16	4.68E-16	0.4088	96,928	14.6707	12,175	1.18E-08	0.0001
700	3.27E-07	0.24			8.3685	0.0334	1.12E-18	1.97E-17	0.0571	46,323	3.8053	3,874,210	2.06E-10	0.0008
Total	2.12E-06	1.53			8.9248	0.0425	2.37E-16	1.36E-15	0.1753	59,536	7.1344	44,321	9.14E-09	0.0004

Sample held at tabulated temperature 60 min for each extraction step. Data normalized to gram weight.

* Indicates atmosphere-corrected excess. Concentration total is the sum of gas released in all steps. Ratio total is the ratio calculated from the concentration totals. Column labeled *R*/Ra (200 °C) lists three sequential isothermal (200 °C; 1 h) measurements of released gas He isotopes.

inclusions are gas rich, as indicated by microscopic examination. Only ppm quantities of O_2, HCl, and HF are detected, and the H_2S/SO_2 ratio is ~2 to 4 consistent with the ratio predicted by the sulfur isotopic data of alunite and coexisting pyrite (Juliani et al., this volume; Rye, this volume). The N_2/Ar ratio ranges from 96.3 for the crush-released to 0.3 and 28.3 for the two thermally released fluid extractions; the weighted total mole and total thermal ratios are 27.5 and 0.44, respectively. These ratios suggest large variations in N_2 and Ar contents but do not imply (especially considering other gas compositions) the presence of atmospheric gas components in the sample, as the N_2/Ar of the present-day atmosphere is approximately 82, and the ratio of N_2/Ar dissolved in air-saturated water is approximately 38. The He content of 214 ppm is high relative to modern atmospheric abundances. The data for Tapajós fluid plot in N_2–Ar–He space as do the data for alunite from the Tambo deposit (Deyell et al., this volume). The ratios of CO_2/CH_4 at 12.8 and H_2S/SO_2 at 2.3 are typical for magmatic-hydrothermal fluids and seem to be equilibrium ratios for fluids at the temperatures of alunite deposition in the Tapajós deposit (Giggenbach, 1997; Juliani et al., this volume). In contrast, the elevated abundances of CO and H_2 are like those of inclusion fluids in other samples of magmatic-hydrothermal alunite (Landis and Rye, this volume). The gas components of these fluids are not in equilibrium, as demonstrated by thermodynamic modeling (Landis and Rye, this volume).

4. Noble gas isotopic data

To define temperature-release profiles for the noble gases, sample X1-16/18 was heated for 60 min at each 100 °C step from 200 to 700 °C, and the extracted gas was analyzed. He, Ne, and Ar isotope compositions of the gases released from this stepwise heating are shown in Table 3. The limited data from this one sample do not allow a precise resolution of each step, but the major trends for the compositions of the

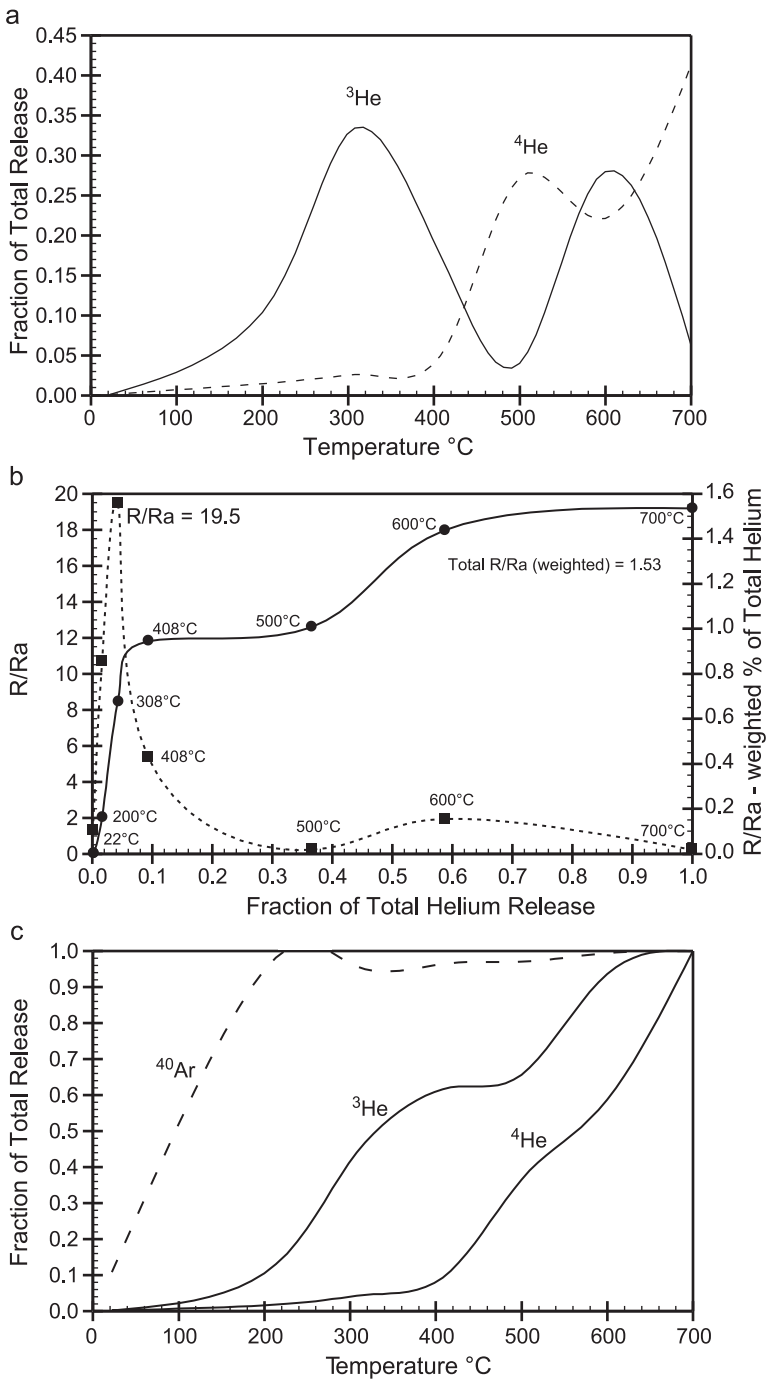

Fig. 2. (a) Temperature-release patterns for ^{3}He and ^{4}He plotted as the percentage of total He measured at a given temperature. Total ^{3}He and ^{4}He release are 2.24×10^{-17} and 1.05×10^{-11} mol g^{-1}, respectively. (b) *R*/Ra (Ra=^{3}He/^{4}He of atmosphere=1.384×10^{-6}) shown as squares and dotted line and *R*/Ra weighted as the percentage of total He released shown as circles and solid line plotted against the fraction of total He released. The temperatures of extraction label each point. *R*/Ra=1.53 for total released He. (c) Fraction of total isotopic species released vs. temperature step for ^{40}Ar, ^{3}He, and ^{4}He.

released gases are easily depicted and interpreted graphically. Figs. 2–5 are plots of specific ratios and multiple isotopes, which are evaluated as indicators of the processes that have affected the noble gases retained in the alunite sample over the past 1.87 b.y.

4.1. Helium and argon isotopes

The isotopic composition of He varies with temperature of extraction (Table 3), and the data for He can be used to indicate the gas sites in X1-16/18. The clear separation, during stepwise heating, of He isotopes with different maxima for ^{3}He, and ^{4}He indicates that the He isotopes are partitioned in multiple sites within alunite. Gas released at ≤200 °C is significantly enriched in ^{3}He (Fig. 2a). The most likely source of this He is the many submicrometer fluid inclusions which host the active gases discussed above and which are almost totally degassed during heating to 200–300 °C. By the 300–408 °C interval and also above the 500 °C temperature of dehydoxylation of alunite, derivation of He from the mineral structure is indicated by the increased amounts of radiogenic ^{4}He (Fig. 2a). The plots of noble gas isotopic temperature profiles define three major sites of gas storage: (1) a fluid inclusion gas site at ≤200 to 300 °C, (2) an OH gas site (alunite mineral dehydration process) at 300 to 500 °C, and (3) an alunite crystal structure gas site (sulfate tetrahedra) at 500 to 700 °C.

For R/Ra, wherein R is $(^3\mathrm{He}/^4\mathrm{He})_{\mathrm{sample}}$ and Ra is $(^3\mathrm{He}/^4\mathrm{He})_{\mathrm{atmosphere}}=1.384\times10^{-6}$, a distinct variation occurs for He released over the range of the temperature profile. Fig. 2b compares R/Ra and the cumulative percentage of total He released with increase in temperature. A maximum R/Ra of 19.5 is reached at 308 °C, but at this temperature, only 4.3% of the total He is released. At 408 °C, R/Ra drops to 5.36, representing 9.3% of total He. The plateau between 408 and 500 °C is at the temperature of initial alunite dehydration, with a large concomitant release of OH and the initial production of H_2SO_4 in the fluid. At 500 °C and above, R/Ra is 0.2 to 2 and is dominated by a high amount of ^{4}He representing nearly 65% of the total He released from the alunite. The weighted sum of R/Ra for the entire temperature-release experiment is 1.53. Helium is released mainly from fluid inclusion sites at lower temperatures and from alunite dehydration and the sulfate structure sites at higher temperatures. Only minor amounts of ^{3}He-rich He are released from fluid inclusions as compared with the abundance of ^{4}He in crystal structure sites.

The temperature profiles of ^{3}He, ^{4}He, and ^{40}Ar are plotted in Fig 2c as the cumulative percentage of total gas released for each isotope vs. temperature. Distinctly different behavior is illustrated by each profile. Approximately 95% of the ^{40}Ar is released during crushing and heating at 200 °C, with nearly continuous release of the remaining 5% occurring from 308 to 700 °C (note that the last 5% of released Ar in this experiment is equivalent to the entire quantity of Ar released in the Ar geochronology experiments described herein; in the geochronology experiments, the extraction system is baked to 260 °C while being pumped to evacuate low-temperature gases, and it is within this temperature range that very large quantities of loosely bound Ar are released). In contrast, ^{3}He shows two temperature ranges of release, one with a maximum around 300 °C and the other with a maximum around 600 °C, with an apparent plateau in between. ^{4}He exhibits only a 10% release up to 400 °C, with the remaining 90% released in a near-monotonic profile over the next 300 °C.

Most of the Ar released between the initial crush and 308 °C is thought to be from fluid inclusions. The ^{40}Ar/^{36}Ar ratio of this large quantity of Ar is 584–629, only slightly radiogenic. Argon released at higher temperatures (≥500 °C) has ^{40}Ar/^{36}Ar ratios to higher than 9.6×10^4, which results from nearly 2 Ga of potassium decay. For these two Ar isotopes, significant mixing between their fluid inclusion and crystal sites did not occur over time or upon release at different temperature intervals. Argon, unlike He, does not show a change in the rate at which it is released during thermal destruction of the OH sites in alunite, thus implying that (1) the Ar (radiogenic ^{40}Ar) released at high temperature is more tightly retained in the K–SO_4 tetrahedrally coordinated site than is the Ar in fluid inclusion sites, and 2) these two sites of Ar retention in alunite are distinctly separate and do not exchange Ar. Argon is released from the breakdown of the tetrahedral sites during the dissociation of K–SO_4 above 600 °C, and it is this Ar that is released during heating for ^{40}Ar/^{39}Ar age spectra. In contrast, release of ^{4}He with increase in temperature is uniform for 90% of the total He released, whereas ^{3}He exhibits

a more varied temperature profile that presumably reflects the presence of discrete ^{3}He-enriched sites. These sites are suspected to be fluid inclusions that have different sizes or different gas/liquid contents and decrepitate at different temperatures.

The contrast in the compositions of noble gases from the different retention sites is evident in Fig. 3a. Helium is a mixture of ^{3}He-enriched He released from fluid inclusions and of radiogenic ^{4}He from the U–Th and K (γ) decay (e.g., spallation-induced ^{4}He production) generated over 1.87 b.y. since the formation of the alunite. The two mixing lines shown in a three-isotope diagram of ^{3}He/^{4}He vs. ^{40}Ar/^{4}He (Fig. 3b) provide evidence for mixing between these He reservoirs within alunite during extraction. The low-temperature steeply sloped mixing line is not strongly dependent upon radiogenic ^{40}Ar but is strongly controlled by He isotopic ratios of the mixed components. The low-slope line is controlled by radiogenic ^{4}He and ^{40}Ar abundances and the ratios of gas released at high temperature.

The slope of the steep line in Fig. 3b reflects mixing of sources for the He initially trapped during deposition of alunite; these sources are He with high *R*/Ra (≈20, very ^{3}He-enriched mantle He) and with *R*/Ra of about 0.02 (crustal He). Mantle noble gases are characterized by ^{4}He/^{40}Ar of approximately 10; the maximum ^{4}He/^{40}Ar calculated for this alunite is about 0.026. The maximum *R*/Ra, i.e., 19.5, may be higher if we were to correct for radiogenic ^{4}He produced from U–Th decay in fluid inclusions. However, our microprobe analyses indicate that mineral U–Th concentrations are below reliable detection limits and must be no more than several tens of ppm; therefore, we conclude that this effect must be small. The potential production of ^{3}He from the neutron-induced reaction on Li [^{6}Li (n, α) ^{3}H→^{3}He] is not likely to be significant because only trace amounts of Li likely are present in alunite.

The low-sloped line in Fig. 3b represents mixed amounts of radiogenic (^{4}He and ^{40}Ar) and possibly some spallogenic ^{3}He and ^{4}He, all of which were released during the heating of the alunite at and above 500 °C. During heating, K–SO_4 structural sites open across the sulfate decomposition temperature. It is speculated that a small amount of spallation ^{3}He accounts for the ^{3}He increase in the 600 °C release. Being deeply embedded in the tetrahedral sites, the ^{3}He is released only upon destruction of the alunite structure (Ozima and Podosek, 2002).

The ^{40}Ar/^{36}Ar ratio of Tapajós X1-16/18 alunite fluid inclusion gas is about 615. This ratio is quite different from the ratio of 97,000 for Ar derived by ^{40}K decay and released from the alunite mineral structure only at higher temperatures. Were ^{40}Ar diffusively mobile over long periods of geological time, fluid inclusion Ar would have exchanged or equilibrated with that of the surrounding host mineral. Even with such an enormous contrast in Ar isotopic composition, this exchange is not evident. Exchange is further ruled out because the alunite ^{40}Ar/^{39}Ar ages are consistent with ages from U-Pb geochronology (Juliani et al., this volume). As observed from the ^{4}He/^{40}Ar plot (Fig. 3a), maximum ^{4}He (α) relative to ^{40}Ar occurs in the 200 to 300 °C range. Although approximately 95% of the total He is released at high temperature, dominantly as radiogenic ^{4}He, the ^{40}Ar accumulated from decay of ^{40}K in the tetrahedrally coordinated K–SO_4 site is more abundant. Clearly, the highly radiogenic ^{40}Ar resides only in the sulfate site and not in the OH site or in fluid inclusions. An otherwise expected crustal production ratio of 4.9 for ^{4}He/^{40}Ar does not apply (^{4}He/^{40}Ar=3.11+0.738 (Th/U)×(U/K)×10^{4} given average U, Th, and K crustal abundance (O'Nions and Ballentine, 1993) in this especially K-enriched alunite environment.

Both ^{36}Ar and ^{38}Ar generally are conservative in a crust-mantle environment, with a terrestrial abundance ratio of ^{38}Ar/^{36}Ar of about 0.187 (Hiyagon et al., 1992; Poreda and Farley, 1992; Honda et al., 1993; Niedermann et al., 1997; McDougall and Harrison, 1999; Ozima and Igarashi, 2000). In a plot of total ^{36}Ar, ^{38}Ar, and ^{38}Ar/^{36}Ar vs. temperature (Fig. 3c), ^{38}Ar/^{36}Ar varies from 3.6 to 14.7 in the 500 to 700 °C steps; the ^{38}Ar/^{36}Ar ratio for low-temperature steps (22–408 °C) is 0.0–0.064. Fluid inclusion and mineral-released Ar below the alunite dehydration temperature interval is extremely enriched in ^{36}Ar. Even Ar released with the OH site breakdown is dominantly ^{36}Ar. Lacking an isotopic fractionation mechanism, we interpret this pattern as high-temperature ^{38}Ar enrichment and low-temperature ^{36}Ar enrichment by an unspecified nuclear process (no isobaric interference of Cl, S, or organic molecules with Ar isotopes were likely to have occurred during the mass spectrometric analyses given the thorough

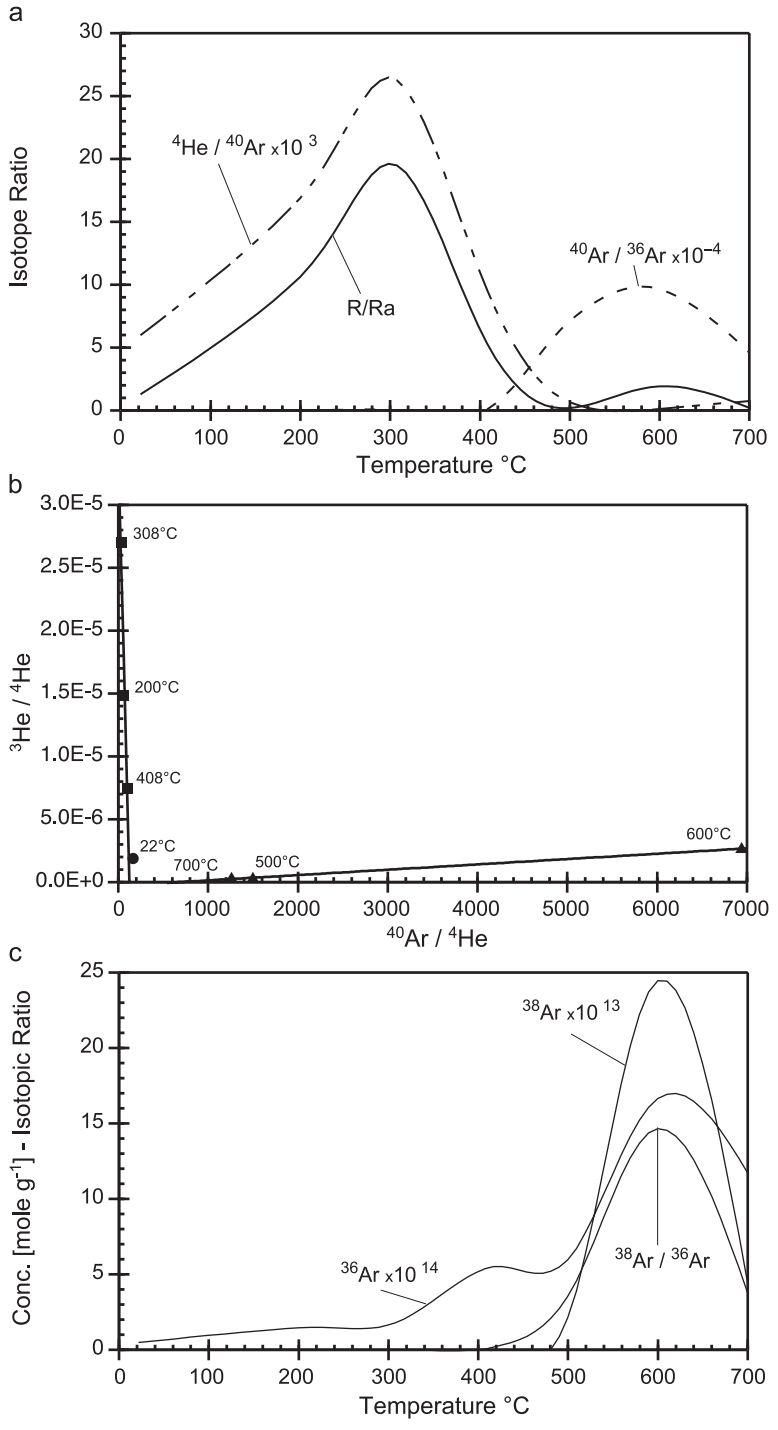
a
Isotope Ratio
^{4}He / ^{40}Ar x10 ^{3}
R/Ra
^{40}Ar / ^{36}Ar x10^{-4}
Temperature °C
b
^{3}He / ^{4}He
308°C
200°C
408°C
22°C
700°C
500°C
600°C
^{40}Ar / ^{4}He
c
Conc. [mole g^{-1}] - Isotopic Ratio
^{38}Ar x10 ^{13}
^{36}Ar x10 ^{14}
^{38}Ar / ^{36}Ar
Temperature °C

cleanup and cryogenic separation procedures that were used).

The observed ^{36}Ar enrichment in fluid inclusions and hydroxylated crystal structure layers is suggested to be from (n, γ) reactions with Cl by plentiful thermal neutrons. The Cl content in the OH sites of this alunite is not known precisely, but several hundred ppm are present (near the microprobe detection limit) as reported in Table 1. In addition, given the likely presence of a trace amount of actinide (U–Th) in the alunite structure and inclusion fluids, with decay-chain production of both fast (>0.1 Mev) and slow to thermal neutrons, typical (n, γ) reactions such as ^{35}Cl (n, γ) ^{36}Cl (β^-) ^{36}Ar and ^{37}Cl (n,γ) ^{38}Cl (β^-) ^{38}Ar are possible. The Q energies of these reactions are large and positive such that only thermal neutrons are required for reactions to proceed. Again, none of the Tapajós alunite was exposed at the surface since formation 1.87 b.y. ago, and cosmogenic neutron production of these Ar isotopes (Renne et al., 2001) is not possible. The maximum effect that the ^{35}Cl (n, γ) ^{36}Cl (β^-) ^{36}Ar reaction could have on the apparent ages of all of the alunite samples analyzed in this study is presented in the following section on Ar geochronology.

From the measured thermal neutron capture cross-sections, the ^{36}Cl/^{38}Cl (and therefore ^{36}Ar/^{38}Ar) production ratio is about 316 (Roddick, 1983). At 500–700 °C, which is sufficiently hot to release Ar from the K–SO_4 sites within the alunite structure, the very large ^{38}Ar enrichment likely is derived from the ^{41}K minor isotope (6.7% abundance) by reaction with slow to fast neutrons according to ^{41}K (n, α) ^{38}Cl (β^-) ^{38}Ar. This (n, α) reaction also would contribute to the radiogenic ^{4}He seen in the gas release at high temperature. An additional pathway, ^{35}Cl (α, p) ^{38}Ar, is possible but is energetically less likely. It is assumed (1) that fluid inclusions contain modified originally trapped Ar, (2) that all atmosphere-corrected excess ^{36}Ar* is derived from the ^{35}Cl pathway (natural $n-\gamma$ reaction in alunite), and (3) in correcting for Cl abundance, the affected Cl concentration is about 37 ppt (atomic). A concentration for total Cl cannot be calculated but will be much higher, given a small increase in ^{38}Ar from ^{37}Cl (1 in 316 Cl atoms) and noting that only a small percentage of Cl atoms will be involved in such nuclear transformations. Probabilities for other nucleogenic production pathways are small because of associated large negative Q energies of reaction.

Tapajós fluid inclusions contain He enriched in ^{3}He and with R/Ra ≈ 20, unlike that of younger magmatic-hydrothermal alunite inclusion fluids reported by Landis and Rye (this volume). Data for He in samples of 10 Ma alunite (Landis and Rye, this volume) show an R/Ra range of 0.07 to 1.31. The unusually high R/Ra in Tapajós alunite almost certainly reflects the age of the occurrence and the derivation of He from a young and less evolved upper mantle source. However, the possibility exists that ^{3}He and ^{4}He had different rates of diffusion, thereby fractionating the He isotopes and yielding an apparent ^{3}He enrichment in the gas released at different temperatures (e.g., R/Ra=19.5). Different diffusion rates for ^{3}He vs. ^{4}He are unlikely because no isotopic fractionation was exhibited for the three sequential isothermal 200 °C heating extractions (Table 3). Moreover, the He thermally released from other samples of alunite with a very different ^{3}He/^{4}He (Landis and Rye, this volume) shows no ^{3}He enrichment relative to crustal values. Because it seems unlikely that He isotopes fractionated as they were released by heating, Ar and Ne likewise would not fractionate during heating experiments in agreement with the conclusions of Trull and Kurz (1999) and Ozima and Podosek (2002).

4.2. Neon isotopes

The intervals of gas release from fluid inclusions, OH, and mineral structural sites are clearly defined in the thermal profiles for Ne in Fig. 4a. Both ^{20}Ne and

Fig. 3. (a) Isotopic ratios vs. temperature step for helium (R/Ra), ^{4}He/^{40}Ar ($\times 10^{3}$), and ^{40}Ar/^{36}Ar ($\times 10^{-4}$). Note that the latter two ratios are multiplied by a scaling factor for illustration purposes. (b) Three-isotope plot of ^{3}He/^{4}He vs. ^{40}Ar/^{4}He showing two mixing lines. Circle (●) is ambient-temperature crush-released gas composition, squares (■) are fluid inclusion gas, and triangles (▲) are alunite structural site gas, respectively. (c) Concentration of ^{38}Ar ($\times 10^{13}$) and ^{36}Ar ($\times 10^{14}$) in mol g^{-1} vs. temperature step and corresponding ^{38}Ar/^{36}Ar ratio clearly define the isotope specific-site release differences for these normally conservative (constant) Ar isotopes. Nuclear (n, γ) and (n, α) reactions involving the isotopes of Cl and K likely produce these differences.

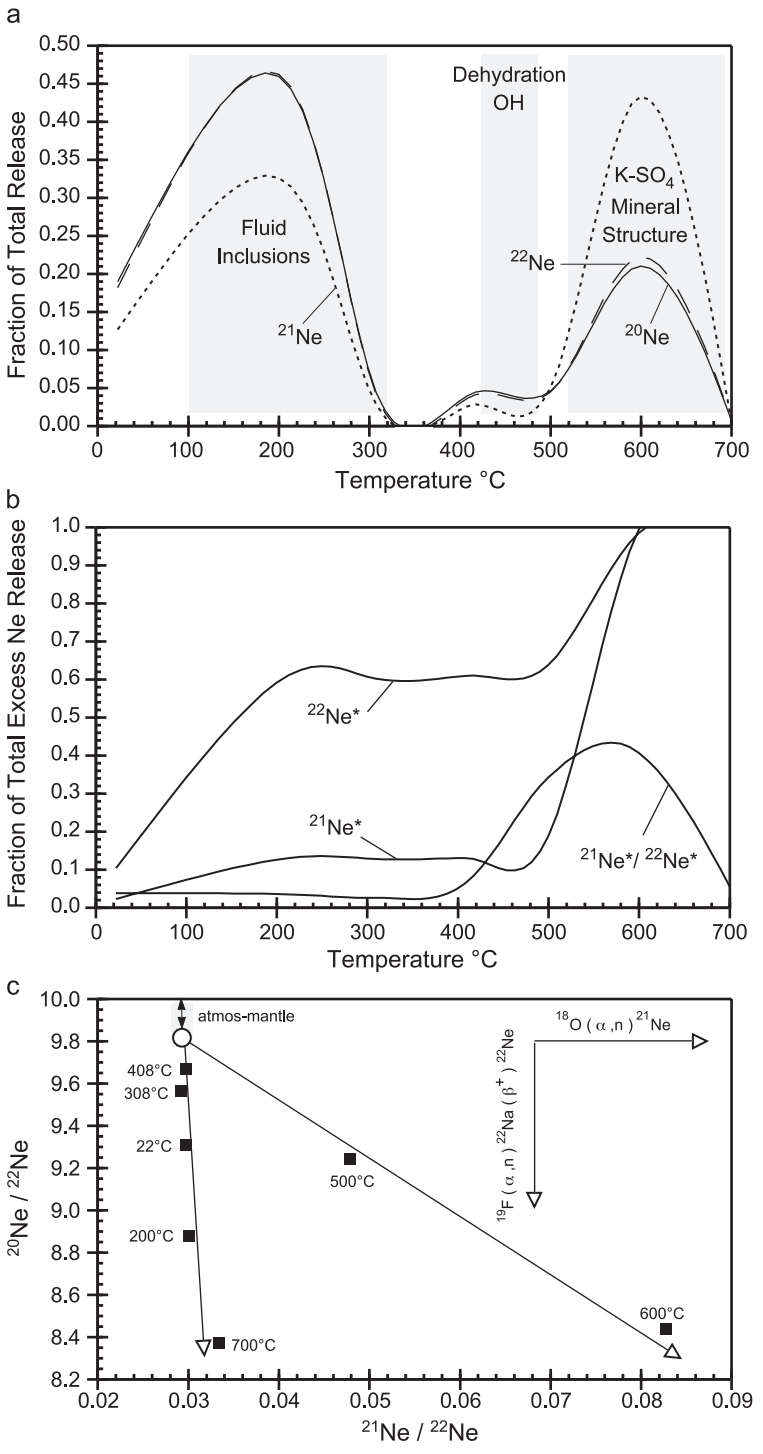
a
Fraction of Total Release
Temperature °C
Dehydration
OH
Fluid
Inclusions
K-SO4
Mineral
Structure
22Ne
21Ne
20Ne
b
Fraction of Total Excess Ne Release
Temperature °C
22Ne*
21Ne*
21Ne*/ 22Ne*
c
20Ne / 22Ne
21Ne / 22Ne
atmos-mantle
408°C
308°C
22°C
200°C
500°C
600°C
700°C
18O (α ,n) 21Ne
19F (α ,n) 22Na (β+) 22Ne

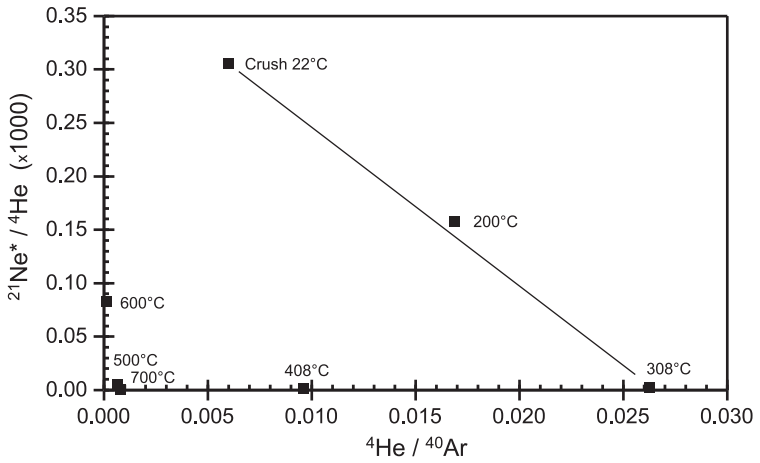

Fig. 5. Three-isotope plot of ^{21}Ne*/^{4}He vs. ^{4}He/^{40}Ar illustrating fluid inclusion population mixing as a separate gas-release site distinguished from higher temperature gas. These data define a constant U–Th–K production ratio in a closed system for fluid inclusion gas.

^{22}Ne exhibit similar thermal profiles from fluid inclusion and dehydration sites. At high temperature, a slight contribution of ^{22}Ne* (excess ^{22}Ne after correction for atmospheric Ne) is observed. The fractions of excess ^{22}Ne* and ^{21}Ne* (corrected for atmospheric Ne and therefore of nucleogenic origins) released by 200 °C are 59.2% and 12.7%, respectively (Fig. 4b). At 600 °C, almost all (98.6% and 99.5%) of the Ne is extracted from the alunite. The ^{21}Ne/^{22}Ne ranges from 0.029 to 0.083, and ^{20}Ne/^{22}Ne ranges from 8.37 to 9.66. Excess ^{21}Ne*/^{22}Ne* is between 0.028 and 0.409 (for reference, ^{21}Ne/^{22}Ne in the atmosphere is 0.029, ^{21}Ne/^{22}Ne in mid-ocean ridge basalts is ≥0.070, and ^{21}Ne/^{22}Ne in Earth's crust is 0.47; Kennedy et al., 1990; O'Nions and Ballentine, 1993; Ballentine, 1997). Lacking any evidence for incorporation of atmospheric gas in the alunite, we infer that the Ne in the alunite is a mixture of mantle and nucleogenic Ne. Neon with an average crustal ^{21}Ne/^{22}Ne value (0.47) results from nucleogenic production in minerals. In Fig. 4c, both ^{21}Ne* and ^{22}Ne* can be seen to reflect derivation from separate fluid inclusion and structural sites. Additionally, ^{21}Ne* dramatically increases preferentially to ^{22}Ne* in the high-temperature release from the K–SO_4 site, giving rise to a peak in the ^{21}Ne*/^{22}Ne* ratio. Significantly more Ne is released only at ≥500 °C, liberating the remaining 36% of ^{22}Ne* and 81% of ^{21}Ne*. The maximum ^{21}Ne*/^{22}Ne* ratio (0.41) is reached at 600 °C.

Fig. 4c illustrates a ^{20}Ne/^{22}Ne–^{21}Ne/^{22}Ne plot of Ne release at each thermal extraction temperature. Isotopically, Ne is a mixture of originally trapped atmospheric (mantle) compositions modified by post-mineral nucleogenic production of ^{21}Ne and ^{22}Ne within the mineral structure. The slope for nucleogenic production shown in Fig. 4c is proportional to ^{19}F/^{18}O within the alunite. Presumably, the α-generating sources are either in fluid inclusions in the OH sites within alunite or are uniformly distributed throughout the crystal structure. Alpha emitters must be in proximity to the appropriate nuclear targets because typical α traveling distances are ~25–40 μm. For example, in granitic rocks, the n/α production ratio is about 2.5×10^{-6}, making (α, n) nuclear production reactions most important in minerals sites

Fig. 4. (a) Fraction of total Ne isotopic species released vs. temperature step for ^{20}Ne, ^{21}Ne, and ^{22}Ne. As seen in the previous diagrams for He and Ar, the Ne clearly defines gas release from fluid inclusions, dehydration OH site, and K–SO_4 mineral structure site. Low-temperature release of Ne exhibits a nearly constant ratio of ^{20}Ne/^{22}Ne and an increased amount of ^{22}Ne at high temperature (lower ^{20}Ne/^{22}Ne). The ^{21}Ne/^{22}Ne has increased to ~0.083 from the near-atmospheric value of 0.029. (b) Fraction of total Ne isotope released vs. the temperature step for calculated ^{21}Ne* and ^{22}Ne* (*indicates atmospheric corrected excess). The excess ^{21}Ne*/^{22}Ne* ratio increased at high-temperature steps through nucleogenic production within the alunite host mineral. (c) Three-isotope plot of ^{20}Ne/^{22}Ne vs. ^{21}Ne/^{22}Ne illustrating the mixing of sites within alunite and the (α, n) nucleogenic reactions with F and O that differently characterize these sites.

Table 4
Data for the step release of Ar isotopes

Temperature [°C]	Step duration (min)	$^{40}Ar_R$	$^{39}Ar_K$	$^{36}Ar_T$	*F*	F_{max}	Age (Ma)	Error±Ma	AI36 (Ma)
X1-16/18 (9.7 mg)									
550	20	4.2549	0.08103	0.00018	52.513	53.166	1750	2	14
600	22	0.4763	0.0093	0.00004	51.482	52.774	1728	9	28
650	20	15.145	0.27174	0.00011	55.735	55.855	1818	2	2
675	21	24.572	0.43128	0.00022	56.975	57.126	1843	2	3
725	23	47.602	0.82307	0.00021	57.835	57.911	1861	2	1
775	21	3.8563	0.06620	0.00011	58.253	58.744	1869	2	9
850	21	0.1285	0.0023	0.00009	55.629	67.126	1816	61	222
1300	40	0.0124	0.0009	0.00016	14.480	69.44	673	24	exc
X1-16/G (10.3 mg)									
500	20	0.0429	0.0023	0.00015	18.396	55.824	822	46	1000
550	40	55.375	0.97529	0.00082	56.778	57.026	1845	2	5
575	20	19.291	0.33867	0.00015	56.961	57.092	1849	2	2.5
600	20	26.824	0.47098	0.00014	56.954	57.041	1849	2	1.5
625	20	11.533	0.20219	0.00003	57.039	57.082	1850	2	1.5
650	24	46.561	0.81387	0.00005	57.209	57.227	1854	2	0.5
675	21	7.2928	0.12750	0.00003	57.199	57.268	1854	2	1.5
700	20	0.6850	0.0134	0.00004	51.197	52.079	1728	17	19
800	20	0.1504	0.0030	0.00007	50.868	57.780	1721	23	144
1000	20	0.0150	0.0014	0.00002	10.516	25.112	514	6	534
X1-16/F (11.3 mg)									
250[a]	915	0.0091	0.0017	0.00297	5.467	534.19	70	8	2788
300	10	0.0503	0.0008	0.00064	65.695	310.94	703	32	1427
400	11	0.0016	0.00006	0.00036	25.015	1800.0	301	56	4467
450	10	0.0012	0.00008	0.00036	15.930	1345.1	197	30	4089
450	20	0.0180	0.0004	0.00043	51.428	414.4	572	11	1932
500	21	0.0628	0.0006	0.00039	103.600	291.88	1011	59	1040
550	11	0.3015	0.0018	0.00038	169.901	233.80	1449	12	341
550	21	1.1762	0.0059	0.00043	199.524	220.89	1615	14	111
575	20	3.7452	0.0167	0.00038	224.314	230.99	1743	5	33
600	20	21.728	0.09414	0.00082	230.789	233.37	1775	7	13
625	20	1.5509	0.00679	0.00047	228.342	248.86	1763	2	98
650	21.5	48.764	0.19753	0.00106	246.866	248.453	1852	2	7
675	21.5	71.107	0.28732	0.00111	247.485	248.616	1855	4	5
725	23	71.918	0.29140	0.00192	246.803	248.740	1852	2	9
800	21	0.7200	0.0031	0.00115	234.639	345.20	1794	14	469
950	25	0.0217	0.0006	0.00087	39.131	506.88	451	5	2333
1200	20	0.0030	0.0007	0.00061	4.146	251.08	53	9	1818
FV3-1/16 (8.3 mg)									
250[a]	695	−0.0005	0.00061	0.00207	−0.89	1000.0	−12	80	3882
450	60	0.0051	0.0001	0.00007	39.67	198.2	472	79	1178
525	24	0.0358	0.0002	0.00006	151.34	247.8	1374	31	527
600	23	2.9703	0.0154	0.00008	193.43	194.9	1623	9	8
675	20	48.016	0.20660	0.00052	232.41	233.1	1827	9	3.5
700	22.5	16.450	0.0694	0.00008	236.98	237.3	1850	15	1.5
725	21	2.1660	0.0091	0.00009	237.64	240.7	1853	26	15
750	23.5	0.2368	0.0010	0.00002	227.81	233.4	1804	21	28
800	24.5	0.3434	0.0017	0.00010	204.13	222.0	1682	11	93
950	20.5	0.0118	0.0004	0.00005	32.742	73.76	398	81	400

Table 4 (*continued*)

Temperature [°C]	Step duration (min)	$^{40}Ar_R$	$^{39}Ar_K$	$^{36}Ar_T$	*F*	F_{max}	Age (Ma)	Error±Ma	AI36 (Ma)
FV3-1/16 (8.3 mg)									
1150	22	0.0250	0.0003	0.00006	76.036	129.4	818	96	411
1350	25.5	0.0419	0.0002	0.00091	243.96	1828.0	1883	30	2978
FV3-1/16 (10.4 mg)									
500	20	11.063	0.23061	0.00051	47.973	48.614	1655	2	14
550	21	9.8095	0.18067	0.00008	54.295	54.426	1792	2	3
575	20	10.154	0.18280	0.00004	55.545	55.609	1818	2	1
600	20	53.307	0.93741	0.00029	56.867	56.958	1845	2	2
625	21	3.6651	0.06420	0.00013	57.092	57.688	1850	2	12
650	21	0.5555	0.0102	0.00003	54.500	55.388	1796	14	19
675	20	0.1151	0.0021	0.00001	54.410	55.700	1794	13	27
700	21	0.1297	0.0025	0.00001	51.543	52.633	1734	14	23
750	20	0.1248	0.0028	0.00005	44.722	50.020	1580	15	120
1000	21	0.0146	0.0034	0.00006	4.278	9.48	227	42	242
FV3-1/11 (11.6 mg)									
205[a]	960	0.0632	0.0056	0.00507	11.317	279.3	523	13	3063
400	19	0.0346	0.0018	0.00068	18.730	127.3	798	31	2025
500	21	0.36830	0.0093	0.00048	39.785	55.091	1408	3	341
550	21	6.0797	0.1549	0.00102	39.253	41.048	1395	12	44
575	20	29.146	0.50582	0.00057	57.622	57.949	1800	2	6
600	20	4.0921	0.06904	0.00067	59.268	62.139	1832	2	55
625	21	141.73	2.3243	0.00129	60.979	61.132	1865	2	3
650	20	2.8361	0.04676	0.00166	60.646	71.142	1859	2	90
675	20	88.623	1.4466	0.00180	61.266	61.627	1871	2	6
700	20	1.9878	0.0326	0.00036	60.880	64.142	1863	4	60
725	20	0.1046	0.0021	0.00053	49.810	124.4	1638	23	1152
800	27.5	0.0041	0.0003	0.00073	14.399	758	643	43	exc
1200	20	0.0019	0.0007	0.00074	2.773	324	143	23	exc
FV3-2/7 (11.7 mg)									
500	22	0.1026	0.0023	0.00015	44.701	63.88	1579	29	403
550	23	13.234	0.25955	0.00019	50.987	51.204	1721	3	5
600	20	62.696	1.11194	0.00002	56.385	56.387	1835	2	0.05
650	25	48.138	0.84323	0.00020	57.087	57.158	1849	2	0.5
675	20	3.5697	0.0623	0.00005	57.280	57.518	1853	5	5
700	35	3.436	0.05975	0.00008	57.504	57.902	1857	2	8
800	32	0.4113	0.0077	0.00007	53.317	56.032	1771	10	56
1250	20	0.0290	0.0013	0.00002	21.607	26.075	932	91	144
FV3-1/25 (9.9 mg)									
500	22	0.0437	0.0011	0.00019	38.790	88.39	1434	33	959
550	20	1.5847	0.03564	0.00007	44.466	45.044	1574	3	13
575	38.5	35.587	0.63959	0.00018	55.641	55.724	1820	2	1.5
600	20	10.867	0.19055	0.00006	57.030	57.123	1848	2	2
625	20.5	0.2147	0.0038	0.00002	56.550	58.060	1838	16	31
650	20	17.616	0.30732	0.00005	57.323	57.370	1854	3	1
675	23	64.373	1.1186	0.00007	57.549	57.565	1859	2	0.3
700	23	2.456	0.04256	0.00005	57.709	58.053	1862	4	7
750	23	0.2786	0.0051	0.00011	54.701	61.131	1800	13	129
1000	20	0.0745	0.0020	0.00009	37.237	50.522	1394	16	317

(continued on next page)

Table 4 (*continued*)

Temperature [°C]	Step duration (min)	$^{40}Ar_R$	$^{39}Ar_K$	$^{36}Ar_T$	*F*	F_{max}	Age (Ma)	Error±Ma	AI36 (Ma)
FV3-1/12 (9.6 mg)									
450	26	0.0196	0.0009	0.00016	22.635	76.90	948	15	1232
525	20	0.0334	0.0014	0.00008	23.750	40.71	984	46	473
600	22	1.2173	0.04009	0.00004	30.363	30.658	1184	1	8
625	20	32.469	0.67332	0.00007	48.222	48.252	1633	2	1
650	21	66.445	1.2228	0.00025	54.339	54.397	1765	2	1
675	20	4.0219	0.07140	0.00007	56.328	56.618	1805	2	6
725	23	2.1886	0.03902	0.00005	56.088	56.467	1800	2	8
800	20.5	0.3920	0.0074	0.00011	52.580	56.976	1728	7	90
1200	20	0.0160	0.0036	0.00010	4.482	11.937	231	9	329
FV3-3/3 (11.9 mg)									
400	21.5	0.0023	0.0005	0.00007	4.655	46.826	244	62	1380
450	22	0.0334	0.0059	0.00021	5.658	16.198	293	15	444
500	19.5	0.0505	0.0182	0.00005	2.781	3.595	150	12	42
525	20	0.10659	0.08247	0.00006	1.293	1.507	71	2	12
550	26.5	0.46165	0.47654	0.00009	0.969	1.080	53.7	0.1	6
575	20	0.50682	0.54896	0.00004	0.923	0.945	51.2	0.1	1
600	20	0.66374	0.71565	0.00003	0.927	0.940	51.4	0.1	0.7
625	33	1.0437	0.82427	0.00009	1.266	1.298	69.8	0.3	2
650	21	0.0992	0.0073	0.00004	13.559	15.182	636	3	63
700	21	0.3797	0.0110	0.00003	34.611	35.418	1320	7	22
1000	21.5	1.6138	0.03995	0.00017	40.399	41.652	1470	2	31

General experimental details are given by Juliani et al. (this volume) and Snee (2002). Sample descriptions are in Juliani et al. (this volume). Abundance of all isotopes including $^{40}Ar_R$ (radiogenic ^{40}Ar), $^{39}Ar_K$ (irradiation-produced K-derived ^{39}Ar), and $^{36}Ar_T$ (total ^{36}Ar) is measured in volts and calculated to five decimal places. Voltage may be converted to moles using 1.160×10^{-12} mol Ar per volt signal. The "*F*" value ($^{40}Ar_R/^{39}Ar_K$) is directly calculated from $^{40}Ar_R$ and $^{39}Ar_K$ in the table. F_{MAX} is calculated by assuming that all measured ^{36}Ar was derived over geological time from the nucleogenic production of ^{36}Ar from chlorine; this value is the maximum possible value for *F*. All isotopic abundances have been corrected for mass discrimination and interfering isotopes created during irradiation. Corrections for Cl-derived ^{36}Ar were determined using the method of Roddick (1983). Production ratios for this experiment are available in Snee (2002). Apparent ages of each fraction include the error in *J* value (0.1%), which was calculated from the reproducibility of splits of the Ar from several standards. Apparent ages were calculated using decay constants of Steiger and Jäger (1977). All apparent age errors are cited at 1σ. Uncertainties in the calculations for apparent age of individual fractions were calculated using equations of Dalrymple et al. (1981). AI36 is the age increase in million years to be added to the apparent age if all measured ^{36}Ar is assumed to be produced from the decay of Cl over geological time; this older apparent age represents the maximum possible age for each temperature step. ^{exc}Age recalculation is excessive.

[a] Argon in breakseal volume.

(Morrison and Pine, 1955). Radiogenic α particles are present in the OH sites, in fluid inclusions, and in the sulfate sites due to U–Th decay and the spallation production of α particles. Kennedy et al. (1990) estimated that about 97% of $^{21}Ne^*$ is derived from O and 98% of $^{22}Ne^*$ from F by the following reactions: ^{18}O (α, *n*) ^{21}Ne, and ^{19}F (α, *n*) ^{22}Na (β^+) ^{22}Ne. The data in Fig. 4c are interpreted as indicating that F (^{19}F) resides in fluid inclusions and as substitutions for OH, and that the Ne in these sites is a mixture of mantle and F-derived nucleogenic Ne. Neon released at high temperature in alunite during stepwise heating is dominated by the ^{18}O (α, *n*) ^{21}Ne reaction (Fig. 4b,c). Fluid inclusion Ne exhibits a low $^{20}Ne/^{22}Ne$, which possibly was created by nucleogenic ^{25}Mg (*n*, α) ^{22}Ne production from Mg solute in the trapped fluids.

Data for Ne, when compared with published MORB and OIB noble gas data (Ozima and Podosek, 2002), indicate that the Ne in the parental fluids of the 1.87-Ga alunite from Tapajós had a composition similar to that of OIB (typical of degassed Proterozoic mantle), with later radiogenic and nucleogenic modifications to the Ne retained in the alunite crystal domains and fluid inclusions. The ^{4}He concentration

and $^{4}He/^{40}Ar$, $^{21}Ne^{*}/^{22}Ne$, and $^{4}He/^{22}Ne$ ratios are on the He-deficient OIB side of a $^{21}Ne^{*}/^{4}He$ production line and are below a closed mantle ^{4}He–^{40}Ar system (Ozima and Igarashi, 2000).

The $^{4}He/^{21}Ne^{*}$ ratio of crush-released and high-temperature thermally released gas (Table 3) is significantly higher than the estimated crustal production of 9.96×10^{-6} (O'Nions and Ballentine, 1993). The large ratios imply the presence of significant radiogenic ^{4}He in the alunite, with noted increases across the temperature intervals for OH loss and the breakdown of K–SO_4 sites. The implication of this observation is that a significant portion of the trace U–Th in alunite resides in the OH sites, as well as within the tetrahedrally coordinated sulfate sites. Both sites favor the buildup of radiogenic ^{4}He from U–Th decay. The $^{21}Ne^{*}/^{40}Ar^{*}$ ratio (Tables 2a,2b), illustrates in-place production of these isotopes after the alunite is formed. The fluid inclusion gases released at <300 °C are characterized by contributions from nucleogenic ^{21}Ne production, and the gases released from structural sites at high temperature are characterized by radiogenic ^{40}Ar.

The geochemical behavior of U and K in the upper mantle-crust creates a constant production ratio of $^{4}He/^{40}Ar$. Both $^{21}Ne^{*}$ and ^{4}He are derived from U and yield a constant $^{21}Ne^{*}/^{4}He$ production ratio (nucleogenic and radiogenic). Assuming the U–Th–K geochemical environment is constant, these production ratios should remain the same, and $^{21}Ne^{*}/^{4}He$ vs. $^{4}He/^{40}Ar$ can be used to evaluate the extent to which the sites of gas retention in alunite have remained closed since formation of the mineral (Fig. 5). For gas released by crushing at ambient temperature and extending through the 308 °C thermal release, the data plot on a straight line that defines a constant production ratio typical of closed system behavior. The isotopic compositions of gas released at higher temperatures plot in a completely different region of the diagram, presumably indicating much different U(Th)–K conditions for the structural gas sites. Examination of the $^{21}Ne^{*}/^{4}He$ changes with temperature (Table 3) reveals increased Ne (α, n) production in structural OH, dominant ^{4}He production in the sulfate sites, and dominant ^{40}Ar production in the higher temperature site(s).

5. Argon geochronological data

Data for Ar thermal release from 10 alunite samples analyzed for Ar age spectra (Juliani et al., this volume) are given, with additional data relevant to this study, in Table 4. These extractions and isotopic analyses were performed in the Denver Ar geochronology laboratory of the USGS on a different vacuum furnace and mass spectrometer system than that used for the rare-gas experiments. Some samples

Table 5
Properties of gas retention sites

Gas retention site	Fluid inclusions	Dehydration layer	K–SO_4 crystal matrix	Reference value[a]
Temperature [°C]	200–300	400–500	500≥700	–
^{3}He %release	44.0	17.6	38.4	–
^{4}He %release	4.3	5.0	90.7	–
$^{21}Ne^{*}$ %release	12.9	0.2	86.8	–
$^{22}Ne^{*}$ %release	60.4	0.7	38.9	–
^{40}Ar %release	0.04	0.21	99.72	–
R/Ra	19.5	5.4	0.2–1.9	Atm.=1; mantle=6.5 to >30; crust ≈ 0.02
$^{40}Ar/^{36}Ar$	615	1017	96,900	Atm.=295.5; mantle=>12000
$^{4}He/^{40}Ar$	0.006–0.026	0.0007	0.0001–0.0008	Mantle=0.05–1000; crustal production=4.9
$^{38}Ar/^{36}Ar$	0.0000–0.002	0.064	3.58–14.67	Atm.–crust=0.188
$^{20}Ne/^{22}Ne$	8.9–9.5	9.7	8.4–9.2	Atm.=9.8; mantle=9.8–13
$^{21}Ne^{*}/^{22}Ne^{*}$	0.028–0.039	0.065	0.057–0.409	Atm.=0.029; mantle >0.070; avg. crust=0.47
$^{21}Ne^{*}/^{4}He$ ($\times10^{7}$)	16–3100	11	3–820	Mantle production=5.9×10^{7}; crust production=1.0×10^{5}
$^{21}Ne^{*}/^{40}Ar$ ($\times10^{-7}$)	0.42–26.5	0.10	0.12–0.002	Crustal production=4.94×10^{-7}

[a] Compiled from O'Nions and Ballentine (1993), Ozima and Podosek (2002), Kennedy et al. (1990), and Yatsevich and Honda (1997).

were baked under vacuum at 250 °C, whereas others were irradiated in individual "breakseals" retaining both the recoil isotopes and the low-temperature gas released from fluid inclusions during bakeout. Although these samples had been irradiated previously in the USGS TRIGA reactor to obtain $^{40}Ar/^{39}Ar$ age determinations, the data and the profiles for temperature release of Ar were examined for additional clues to the retention and diffusion of Ar in alunite and for possible in-place nucleogenic modifications (Table 5).

The results of the "breakseal" experiments indicate that less than 1 part in 500 of ^{39}Ar and less than 1 part in 5000 of ^{40}Ar were released into the vacuum during irradiation and subsequent heating during bakeout. Not listed in Table 4 are the large unquantified volumes of generally atmospheric ^{40}Ar, ^{38}Ar, and ^{36}Ar released from the sample into the breakseal volume during the bakeout. This Ar likely is equivalent to the 95% of the Ar that was released from fluid inclusions during the noble gas crushing and thermal extraction experiments on X1-16/18 alunite.

Just as ^{38}Ar and ^{36}Ar are produced from nucleogenic reaction in the natural environment, these isotopes are also produced during irradiation. The reactions of interest are the same as those in the natural environment, i.e., ^{35}Cl (n, γ) ^{36}Cl (β^-) ^{36}Ar and ^{37}Cl (n, γ) ^{38}Cl (β^-) ^{38}Ar. The samples were analyzed too quickly after irradiation to detect any ^{36}Ar produced from Cl. These measurements, however, say nothing about the production of ^{38}Ar and ^{36}Ar from nucleogenic reactions over geological time. The implications of nucleogenic production of ^{36}Ar from Cl over the life of the alunite are discussed below.

Fig. 6 is a plot of the cumulative percentage of ^{39}Ar released from 400 to 850 °C for all alunite samples. As shown in Table 4, the majority of all Ar is released from the samples within a small part of this range. In all cases, more than 99% of the Ar isotopes are released between 525 and 725 °C regardless of compositional (Table 1) or textural (Fig. 1) variation. For all samples, more than 95% of the Ar is released over a 125 °C interval between 525 and 725 °C. It was not uncommon for 40% or more of the ^{39}Ar to be released in a single 25 °C step within this 525–725 °C span. Because alunite undergoes OH loss near 500 °C, the release of more than 99% of the radiogenic Ar above 525 °C shows the lack of relationship to OH loss. Instead, degassing of Ar is likely related to K–SO_4 structural breakdown above 600 °C. The release patterns indicate a direct association of radiogenic and reactor-produced Ar within the K–SO_4 sites. However, it is surprising that little or no Ar is released during dehydroxylation.

The $^{40}Ar/^{39}Ar$ age spectra of the eight samples discussed here and in Juliani et al. (this volume) show apparent ^{40}Ar loss exhibited by an increase in apparent age with increase in the percentage of ^{39}Ar

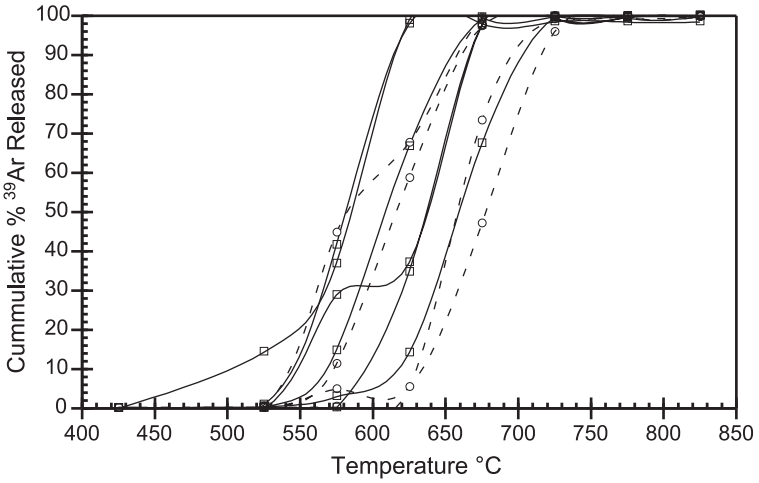

Fig. 6. Cumulative percentage of ^{39}Ar released from all alunite samples. More than 99% of the Ar is released between 525 and 725 °C.

released. The amount of apparent Ar loss is greatest for FV3-1/12, a sheared alunite. The other seven samples exhibit <1% to a few percent of apparent Ar loss, and five of the samples exhibit plateaus or near plateaus with apparent ages ranging from 1846±2 (1σ) Ma to 1867±2 Ma. Although many of these plateau ages are distinct, there is no clear age relationship to alunite generation (Juliani et al., this volume). The first generation and apparently the paragenetically oldest of the alunite samples (FV3-1/16 and FV3-1/11) exhibits the two extreme ages of 1846 and 1867 Ma (respectively). Though Juliani et al. (this volume) note that hydrothermal events producing later generations of alunite exhibiting crosscutting and replacement textures did not seem to alter the compositions of the earlier formed alunite, perhaps some minor amount of radiogenic Ar was lost.

Two separately collected and analyzed samples from the same FV3-1/16 locality gave a $^{40}Ar/^{39}Ar$ age-spectrum plateau date of 1834±17 Ma defined by 95.7% of the released ^{39}Ar and a plateau date of 1845±2 Ma defined by 62% of the released ^{39}Ar. Although these dates are identical within analytical error, the analyses reveal differences that are important for understanding the effects of different analytical procedures. The apparent age with the larger error represents the original sample used to determine whether Precambrian alunite could retain radiogenic Ar over its geological history. Prior to this analysis, the oldest published date from alunite was 62 Ma (Bird et al., 1990). With the expectation that Precambrian alunite would have lost substantial radiogenic Ar, the first alunite sample was subjected to only a 30 h of irradiation at 1 MW, which resulted in a $^{40}Ar_R/^{39}Ar_K$ ratio of ~240. An 8-mg sample size and our instrument sensitivity yielded $^{39}Ar_K$ abundances too small to give optimal statistics. In addition, this sample was degassed in a manner in which nearly 75% of the ^{39}Ar was released in the step at 675 °C. However, this reconnaissance experiment was encouraging, and it justified the analysis of additional alunite samples from the deposit. For the second experiment, all but one sample was irradiated for 129 h at 1 MW, resulting in $^{40}Ar_R/^{39}Ar_K$ ratios of approximately 60, with $^{39}Ar_K$ abundances that produced analytical errors improved by an order of magnitude. In the second experiment on FV3-1/16, the degassing schedule was performed in more detail.

Nonetheless, some of the differences between the two experiments are not fully reconcilable solely by the difference in experimental techniques. In the second experiment, the majority of the ^{39}Ar was released at or before 600 °C; in the first, Ar was released between 675 and 700 °C. The cause of this difference is unclear, but one possibility is that in twice sampling from the same locality, alunite of slightly different compositions and grain sizes was selected. Juliani et al. (this volume) discuss within-sample variably of alunite and show convincingly that compositional and textural variation is common in single samples. In calculating the diffusion parameters below and in examining the temperature-release profiles, it was noted that the first analyzed FV3-1/16 alunite fits one group of alunite, whereas the other FV3-1/16 alunite exhibits properties characteristic of a second group.

As discussed above, natural nucleogenic reaction on Cl, i.e., $^{35}Cl\ (n, \gamma)\ ^{36}Cl\ (\beta^-)\ ^{36}Ar$, can produce a significant amount of ^{36}Ar within the alunite over geological time. In the typical $^{40}Ar/^{39}Ar$ age-reduction program, it is assumed that all nonreactor-produced ^{36}Ar (i.e., ^{36}Ar that is not produced by nuclear reactions on Cl or Ca during irradiation) is atmospheric. The amount of atmospheric ^{36}Ar calculated is used to correct for atmospheric ^{40}Ar. If some of the ^{36}Ar attributed to atmospheric contribution were instead derived by nucleogenic production of ^{36}Ar from Cl within the alunite over geological time, too large a correction for the atmospheric contribution would be applied. In Table 4, F_{MAX} (where F is $^{40}Ar_{Radiogenic}/^{39}Ar_{Potassium}$) has been calculated by assuming, as an upper end member, that all ^{36}Ar assignable to atmospheric Ar correction was in fact produced by Cl nucleogenic reaction. This F_{MAX} is used to calculate an age correction. In some cases, the age increase is significant. However, for most radiogenic fractions, the age increase is 1 to 5 m.y., which is insignificant in the calculated age of each sample.

6. Diffusion models

The data from the experiments of gas release from alunite during stepped heating, along with the

interpretation of the geochemical framework as presented above, are used to model diffusion parameters and Ar and He retention within alunite. If the gas in question were uniformly distributed or approximately so and if simple volume diffusion occurred during the release of the gas from the alunite, an Arrhenius plot [log (D) vs. $1/T$] of the data would define diffusion activation energy and log (D) as a f (temperature). The calculation requires that (1) the phase remains stable throughout the extraction experiment, which is true for radiogenic ^{40}Ar above 500 °C but not for ^{4}He, (2) the initial distribution of gas be uniformly distributed, which again is not necessarily a good assumption except for ^{40}Ar, (3) alunite crystal shape approximates that selected (spherical) for the diffusion equation, and (4) it is possible to determine the effective diffusion length (radius). Volume diffusion (characterized by length parameter) is the limiting step, with surface diffusion along crystal boundaries and major cleavage or fractures proceeding rapidly once a gas molecule reaches the outer edge of a crystal. Other species, such as ^{3}He and Ne isotopes, were not modeled because only ^{4}He and ^{40}Ar showed smooth release curves as f (time), with the bulk of the gas released near or above the dehydroxylation temperature and therefore best approximating the above criteria. Neon isotopes theoretically should behave much like those of Ar.

Because of the concern about possible isotopic fractionation by diffusion, thereby resulting in the release of He with high ^{3}He/^{4}He from the alunite fluid inclusion sites, ^{3}He was compared with ^{4}He in the initial examination. Theoretically, ^{3}He diffusion parameters should be at most only 8% more rapid than those of ^{4}He; that is, isotopic partitioning is proportional to $m^{-0.5}$, and for a mass difference δm, the δm/m fraction is small. If applied in the energy term, this yields a proportional theoretical difference in diffusion of 1−0.25 (δm/m) or 0.9167. Thus, a large isotopic fractionation of ^{3}He from ^{4}He via diffusion out of alunite structural sites is not expected. The conclusion is that the measured ^{3}He/^{4}He value from the fluid inclusion site (R/Ra=19.5) is real, and that variation in the release of ^{3}He compared with ^{4}He is due to inhomogeneous site-specific compositions (Fig. 2c).

A spherical approximation was utilized to calculate the fractional loss of a gas species (f) as a function of Dt/r^2 (Fechtig and Kalbitzer, 1966; McDougall and Harrison, 1999), where D is the diffusion coefficient, t is time, and r is the radius. The model calculations are sensitive to the radius as the dimensional parameter for volume diffusion (r is assumed to be 10 μm, as in 3.1.2). The Arrhenius plot for ^{3}He and ^{4}He behavior is illustrated in Fig. 7. The ^{3}He is discounted on the grounds that it is not

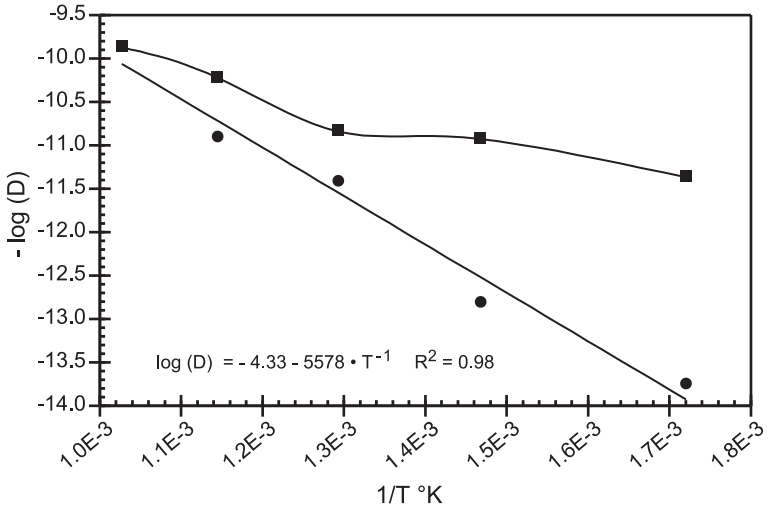

Fig. 7. Arrhenius plot from step-heating data for ^{3}He (■) and ^{4}He (●) with linear regression equation for ^{4}He. The ^{3}He regression is not calculated because ^{3}He is not uniformly distributed in the alunite and therefore does not satisfy essential criteria for the valid analysis of diffusion parameters. The ^{4}He log (D_0)=−4.329 and activation energy E=106.8 (kJ mol^{-1}).

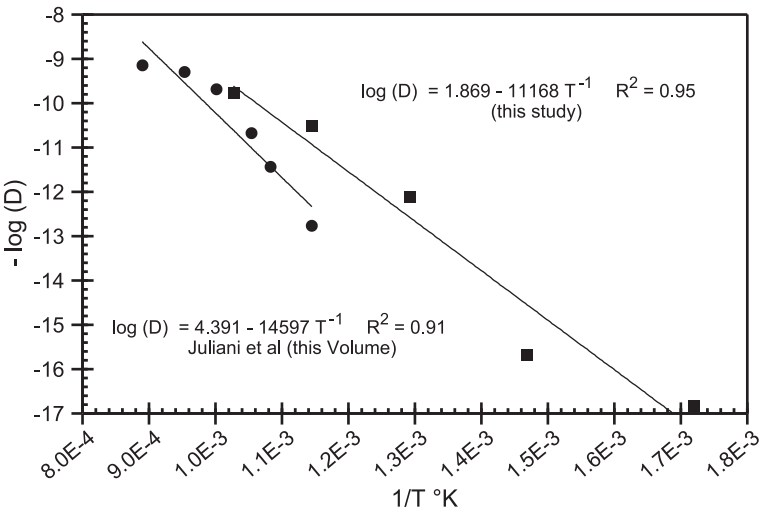

Fig. 8. Arrhenius plot from step-heating data for ^{40}Ar obtained in this study (■) extending to lower temperature than the data derived from the age-spectra release of ^{40}Ar in the geochronology analysis (●) of an irradiated split from the same sample (X1-16/18, Juliani et al., this volume). Results are comparable with ^{40}Ar log (D_0)=1.869 and 4.391 and activation energies E=213.8 and 279.5 kJ mol^{-1}, respectively. When combined with the analysis of other age-spectra release data (Table 4), the results define two alunite populations on the basis of their diffusion parameters and other criteria.

uniformly distributed throughout the alunite but occurs predominantly in fluid inclusion sites. Fig. 8 compares an Arrhenius plot of ^{40}Ar released from splits of the Tapajós X1-16/18 alunite that were analyzed both in the noble gas and the age experiments. The results of these analyses and from all other analyses of Ar age spectra are in Table 6a. The diffusion parameters for each analysis are ordered according to oldest to youngest mineralization events (Juliani et al., this volume).

Table 6a
Alunite diffusion properties

Noble gas experiment	Log (D_0)	Slope E/(2.303*R)	E (kJ mol^{-1})	Comments				
	Step heating: Tapajós X1-16/18			Arrhenius Eq. log (D)=log (Do)+E/(2.303R)(1/T)				
Helium-4	−4.3285	−5578	106.81					
Helium-3	−7.8480	−2101	40.23					
Argon-40	**1.8689**	**−11168**	**213.84**					
Argon geochronology	Age spectra extractions			Gen[a]	δ^{34}S	T (°C)	Age (Ma)	Location
FV3-1/11	14.5790	−22964	439.69	B_1	15.8	260	1867	DH1 (55.1m)
X1-16/18	**4.3910**	**−14597**	**279.49**	A_4	26.7	250	1869	Surface
FV3-1/25	15.4240	−24000	459.53	B_2	14.0	420	1858	DH1 (129.8m)
FV3-2/7	**−0.0887**	**−9359**	**179.19**	B_2	21.4	280	1857	DH2 (127.8m)
X1-16F	16.8140	−25769	493.40	A_3	14.3	420	1853	Surface
X1-16G	**1.8764**	**−10774**	**206.29**	A_2	38.2	130	1851	Surface
FV3-1/16 (1)	**2.6257**	**−11247**	**215.35**	B_1		300	1846	DH1 (70.9m)
FV3-1/16 (2)	16.2560	−25643	490.99	B_1	18.2	300	1846	DH1 (70.9m)
FV3-1/12	13.5650	−22972	439.85	Rxlz	12.4	–	1805	DH1 (58.2m)
FV3-3/3	**4.0056**	**−13345**	**255.52**	SG	4.1	–	51.3	DH3 (66.7m)

DH—drill hole, Rxlz—recrystallized, SG—supergene. Samples in bold type have low activation energy diffusion parameters as discussed in text. Samples FV3-1/16 (1) and (2) are not duplicate analyses but are of alunite samples collected separately at the same locality.

[a] Alunite generation, δ^{34}S, δ^{34}S (alunite–pyrite) calculated T °C, and Ar age are as described in Juliani et al. (this volume).

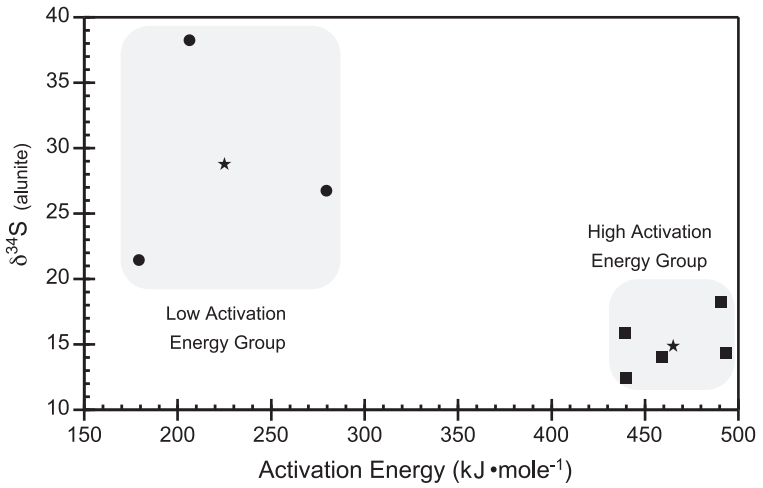

Fig. 9. Comparison of the two alunite groups on the basis of calculated activation energies and $\delta^{34}S$ of the alunite sulfate–sulfur (Juliani et al., this volume). Parameters characterizing alunite with different diffusion coefficients for noble gases in alunite from Tapajós are given in Table 6b. Cross symbol is the average of each group cluster. Fundamentally important differences between the groups with high activation energy and low activation energy likely are not the $\delta^{34}S$ or implied temperature from $\Delta\delta^{34}S$ (alunite–pyrite) but instead are the contrasting solid–solution compositions.

The data for alunite segregate into two groups of diffusion parameters, with average activation energies of 225 and 465 kJ mol^{-1}. There is no correlation with age, geological occurrence and paragenetic grouping (A_1–A_5 or B_1–B_3 alunite), texture, composition, or simple attributes other than the crystallinity and fluid inclusion morphology and placement within the alunite. However, it is possible that the two groups correlate with the chemical compositions of the alunite. In support of this possibility, the activation energy of each group shows a different range of $\delta^{34}S_{(alunite)}$ values and a different range of temperatures calculated from the sulfur-isotope data of coexisting alunite and pyrite (Fig. 9). The sulfur-isotope study of Juliani et al. (this volume) is preliminary. The difference in activation energies for noble gas diffusion seems to reflect temperatures of deposition of alunite but more fundamentally reflect the differences in composition (Table 6b).

Table 6b
Average diffusion properties of two alunite groups

Alunite	Arrhenius Eq.	Activation energy [kJ mol^{-1}]	$\delta^{34}S$ [‰]	Temperature [°C] (alunite–pyrite)
Low *E*	Log (*D*)=2.4465–11748.3 (1/*T*)	225	28.8	240
High *E*	Log (*D*)=15.3276–24269.6 (1/*T*)	465	14.9	350

The diffusion coefficients thus calculated support the published assertion by other workers that alunite reliably retains Ar for geochronological purposes. The diffusion coefficients and activation energies of Ar and He as obtained in this study of alunite are similar to those obtained by others for various other host minerals (Lippolt and Weigel, 1988; Trull et al., 1991; Trull and Kurz, 1999; Ozima and Podosek, 2002).

Taking the derived diffusion coefficients for ^4He and ^{40}Ar in alunite, we model the simplistic 1/*e*–folding time based upon a spherical model and a range of effective radii. The calculated time plotted as a function of temperature (Fig. 10) is the time it takes to lose 1/*e* (0.3679 or roughly 1/3) of the uniformly distributed ^4He and ^{40}Ar from a sphere of specified radius. The high-value diffusion constants of He and Ar in alunite have been used to model the loss as a limiting case, as almost no Ar is lost using the low-value parameters (Fig. 10). It is concluded from these calculations that ^4He is easily retained in alunite at or below 100 °C, and ^{40}Ar is retained at or below 200–220 °C. Diffusion distance for an infinite half-sheet

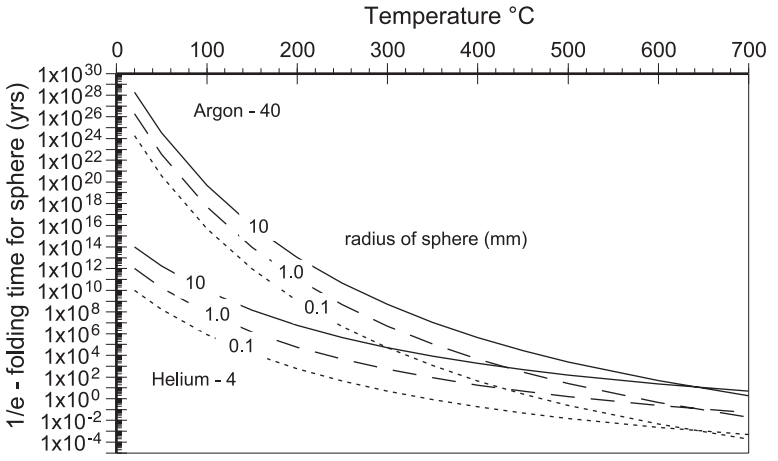

Fig. 10. Model calculation of time to diffuse a 1/*e*–folding amount of ^{40}Ar and ^{4}He from a modeled sphere of alunite, using the higher diffusion parameters for noble gas in alunite at sphere radii of 0.1 to 10 mm. Helium is retained at $T \leq 100$ °C and Ar at $T \leq 200$–220 °C as an approximate assessment.

geometry at ages from 1 Ma to 1 Ga are modeled in Fig. 11. Helium should remain in alunite for millions of years at temperatures of <100 °C, whereas at <200 °C, the Ar should remain almost indefinitely.

7. Conclusions

The patterns of gas compositions of fluids released by crushing and thermal degassing at 200 °C, as well as step heating to 700 °C, are a reflection of the three major gas retention sites in alunite: (1) fluid inclusions, (2) OH site, and (3) sulfate site. Gases extracted from each of these sites have distinct compositions, and there seems to be little mixing of gases among these sites. During heating, gases are quantitatively released at about 200 °C from fluid inclusions at 400–500 °C from the OH sites and at 500–700 °C from the sulfate sites. Maximum Ar release at ~700 °C is observed in alunite age-spectrum data (Table 4; Juliani et al., this volume). Analyses of noble gases extracted from 1.87-Ga alunite record isotope values of a

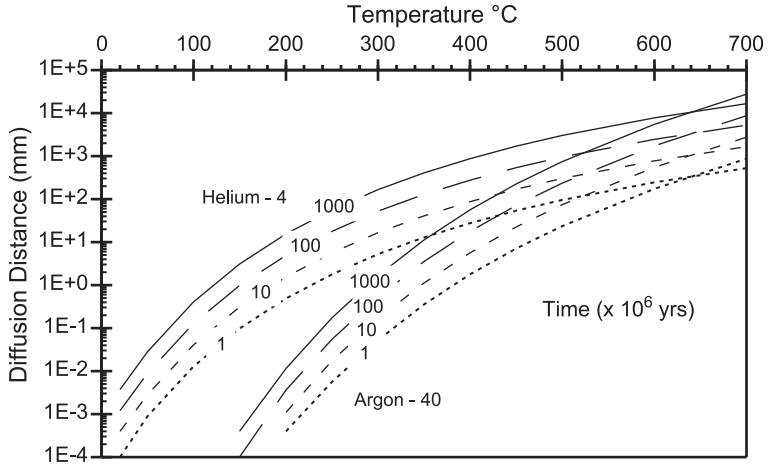

Fig. 11. Model diffusion distances calculated using highest diffusion coefficients for noble gas in alunite assuming an infinite half-sheet and times of 1 Ma to 1 Ga.

primitive and relatively undegassed mantle (magmatic) component in fluid inclusion sites and record in the mineral matrix a postentrapment component that has evolved isotopically through radiogenic and nucleogenic processes.

The *R*/Ra ratio of 19.5 for He in inclusion fluids indicates a less degassed mantle component similar to that of a mantle hot spot (OIB) or more primitive mantle. The fluid inclusions have preserved He with a mantle signature and probably have preserved gases whose composition reflects that of the parental fluids for magmatic-hydrothermal alunite that formed at 1.87 Ga. Gases released during the step heating of alunite have distinct active and noble gas sites. Gases in fluid inclusions seem to retain their original composition from the time of trapping and are subsequently modified by in situ radiogenic and nucleogenic reactions rather than by diffusional loss to or the addition of gases from the surrounding crystal matrix. Radiogenic ^{40}Ar and ^{4}He are preserved in the sulfate site in the alunite crystal structure during heating even to above mineral dehydroxylation, with maximum gas release occurring at about 600 °C. Calculated diffusion parameters for He and Ar are consistent with the analytical results. Helium and Ar diffusion coefficients and activation energies indicate that the composition of both gases should remain largely unexchanged in alunite for ≥100 m.y. at temperatures below 100 °C, which is consistent with the observation that alunite is an excellent K-bearing host mineral for Ar geochronology applications, with 'closure temperatures' of approximately 200 °C. Submicrometer fluid inclusions in alunite should provide useful geochemical information about the gases that were present in the fluids at the time of alunite crystallization.

Acknowledgements

We thank the USGS staff members A.G. Hunt and L. Mills-Herring for their assistance in the gas step-heating experiments, Amy Bern for microprobe analyses of alunite samples, and Ross Yeoman for conducting many of the Ar extractions. The many discussions with Robert Rye and his insightful reviews greatly improved the manuscript. We also acknowledge the helpful reviews by Albert Hofstra, John Chesley, and J.K. Böhlke. The many contributions by Carmen M.D. Nunes and Rafael H. Corrêa Silva that expanded our understanding of the geological framework of Tapajós alunite are gratefully acknowledged. We thank the Fundação de Amparo à Pesquisa do Estado de São Paulo, PRONEX/CNPq/UFPA, and the Conselho Nacional de Pesquisa for the support and access to the Tapajós deposits. The well-developed geological context of the Tapajós gold district and the antiquity and magmatic-hydrothermal volcanic setting of these geologically undisturbed high-sulfidation alunite samples have proved crucial to our efforts to evaluate active and noble gas behavior in alunite. **[PD]**

References

Ashley, R.P., Silberman, M.L., 1976. Direct dating of mineralization at Goldfield, Nevada, by potassium–argon and fission-track methods. Econ. Geol. 71, 904–924.

Ballentine, C.J., 1997. Resolving the mantle He/Ne and crustal $^{21}Ne/^{22}Ne$ in well gases. Earth Planet. Sci. Lett. 152, 233–249.

Bird, M.I., Chivas, A.R., McDougall, I., 1990. An isotopic study of surficial alunite in Australia: 2. Potassium–argon geochronology. Chem. Geol. 80, 133–145.

Brophy, G.P., 1960. Sulfate studies: (Part) 1. Alunite–jarosite solid solution. Geol. Soc. Amer. Bull. 71, 1834–1835.

Brophy, G.P., Scott, E.S., Snellgrove, R.A., 1962. Sulfate studies: (Part) 2. Solid solution between alunite and jarosite. Am. Mineral. 47, 112–126.

Cunningham, C.G., Rye, R.O., Steven, T.A., Mehnert, H.H., 1984. Origins and exploration significance of replacement and vein-type alunite deposits in the Marysvale volcanic field, west central Utah. Econ. Geol. 79, 50–71.

Dalrymple, G.B., Alexander, E.C., Lanphere, M.A., Kraker, G.P., 1981. Irradiation of samples for $^{40}Ar/^{39}Ar$ dating using the Geological Survey TRIGA reactor. U. S. Geol. Surv. Prof. Pap. 1176 (55 pp.).

Dammer, D., 1995. Geochronology of chemical weathering processes in the northern and western Australian regolith. PhD thesis, Australian National Univ., Canberra.

Deyell, C.L., Rye, R.O., Landis, G.P., Bissig, T., this volume. Alunite and the role of magmatic fluids in the Tambo high-sulfidation deposit, El Indio-Pascua belt Chile. Chem. Geol.

Fechtig, H., Kalbitzer, S., 1966. The diffusion of argon in potassium-bearing solids. In: Schaeffer, O.A., Zahringer, J. (Eds.), Potassium Argon Dating. Springer-Verlag, Berlin, pp. 68–107.

Fielding, S.J., 1981. Crystal chemistry of the oxonium alunite–potassium alunite series. MS Thesis, Lehigh University, Bethlehem, Pennsylvania.

Fielding, S.J., Sclar, C.B., 1980. The oxonium alunite–potassium alunite series; synthesis and characterization. Abstr. Programs-Geol. Soc. Am. 12 (7), 425.

Giggenbach, W.F., 1997. The origin and evolution of fluids in magmatic-hydrothermal systems. In: Barnes, H.L. (Ed.), Geochemistry of Hydrothermal Ore Deposits. 3rd ed. Wiley, New York, pp. 737–796.

Kennedy, B.M., Hiyagon, H., Reynolds, J.H., 1990. Crustal neon: a striking uniformity. Earth Planet. Sci. Lett. 98, 277–286.

Hiyagon, H., Ozima, M., Marty, B., Zashu, S., Sasaki, H., 1992. Noble gases in submarine glasses from mid-oceanic ridges and Loihi seamount: constraints on the early history of the Earth. Geochim. Cosmochim. Acta 56, 1301–1316.

Honda, M., McDougall, I., Patterson, D.B., Doulgeris, A., Clague, D.A., 1993. Noble gases in submarine pillow basalt glasses from Loihi and Kilauea, Hawaii: a solar component in the Earth. Geochim. Cosmochim. Acta 57, 859–874.

Juliani, C., Rye, R.O., Nunes, C.M.D., Snee, L.W., Corréa Silva, R.H., Monteiro, L.V.S., Bettencourt, J.S., Neumann, R., Neto, A.A., this volume. Paleoproterozoic high-sulfidation mineralization in the Tapajós gold province, Amazonian Craton, Brazil: geology, mineralogy, alunite argon-age and stable-isotope constraints. Chem. Geol.

Landis, G.P., Hofstra, A.H., 1991. Fluid inclusion gas chemistry as a potential minerals exploration tool: case studies from Creede, CO, Jerritt Canyon, NV, Coeur d'Alene district, ID and MT, southern Alaska mesothermal veins, and mid-continent MVT's. J. Geochem. Explor. 42, 25–59.

Landis, G.P., Rye, R.O., this volume. Characterization of gas chemistry and noble-gas isotope ratios of inclusion fluids in magmatic-hydrothermal and magmatic-steam alunite. Chem. Geol.

Lippolt, H.J., Weigel, E., 1988. ^{4}He diffusion in ^{40}Ar-retentive minerals. Geochim. Cosmochim. Acta 52, 1449–1458.

McDougall, I., Harrison, T.M., 1999. Geochronology and Thermochronology by the ^{40}Ar/^{39}Ar Method. 2nd ed. Oxford Univ. Press, Oxford, UK.

Morrison, P., Pine, J., 1955. Radiogenic origin of helium isotopes in rock. Ann. N. Y. Acad. Sci. 62, 71–79.

Niedermann, S., Bach, W., Erzinger, J., 1997. Noble gas evidence for a lower mantle in MORBs from the southern East Pacific Rise: decoupling of helium and neon isotope systematics. Geochim. Cosmochim. Acta 61, 2697–2715.

O'Nions, R.K., Ballentine, C.J., 1993. Rare gas studies of basin scale fluid movement. Philos. Trans. R. Soc. Lond. 344, 141–156.

Ozima, M., Igarashi, G., 2000. The primordial noble gases in the Earth: a key constraint on Earth evolution models. Earth Planet. Sci. Lett. 176, 219–232.

Ozima, M., Podosek, F.A., 2002. Noble Gas Geochemistry. 2nd ed. Cambridge Univ. Press, Cambridge, UK.

Poreda, R.J., Farley, K.A., 1992. Rare gases in Samoan xenoliths. Earth Planet. Sci. Lett. 113, 129–144.

Renne, P.R., Farley, K.A., Becker, T.A., Sharp, W.D., 2001. Terrestrial cosmogenic argon. Earth Planet. Sci. Lett. 188, 435–440.

Roddick, J.C., 1983. High precision intercalibration of ^{40}Ar–^{39}Ar standards. Geochim. Cosmochim. Acta 47, 887–898.

Roedder, E., 1984. Fluid inclusions. Rev. Mineral. 12 (644 pp.).

Rye, R.O., this volume. A review of the stable-isotope geochemistry of sulfate minerals in selected igneous environments and related hydrothermal systems. Chem. Geol.

Rye, R.O., Bethke, P.M., Wasserman, M.D., 1992. The stable isotope geochemistry of acid sulfate alteration. Econ. Geol. 87, 225–262.

Slansky, E., 1973. The thermal investigation of alunite and natroalunite. Neues Jahrb. Mineral., Monatsh., 124–138.

Snee, L.W., 2002. Argon thermochronology applied to mineral deposits—a review of analytical methods, formulations, and selected applications. U.S. Geol. Surv. Bull. B2194 (39 pp.).

Steiger, R.H., Jäger, E., 1977. Subcommission on Geochronology: convention on the use of decay constants in geo- and cosmochronology. Earth Planet. Sci. Lett. 36, 359–362.

Trull, T.W., Kurz, M.D., 1999. Isotopic fractionation accompanying helium diffusion in basaltic glass. J. Mol. Struct. 485–486, 555–567.

Trull, T.W., Kurz, M.D., Jenkins, W.J., 1991. Diffusion of cosmogenic ^{3}He in olivine and quartz: implications for surface exposure dating. Earth Planet. Sci. Lett. 103, 241–256.

Vasconcelos, P.M., 1999. K–Ar and ^{40}Ar/^{39}Ar geochronology of weathering processes. Annu. Rev. Earth Planet. Sci. 27, 183–229.

Vasconcelos, P.M., Brimhall, G.H., Becker, T.A., Renne, P.R., 1994. ^{40}Ar/^{39}Ar analysis of supergene jarosite and alunite: implications to the paleoweathering history of the western USA and West Africa. Geochim. Cosmochim. Acta 58, 401–420.

Yatsevich, I., Honda, M., 1997. Production of nucleogenic neon in the earth from natural radioactive decay. J. Geophys. Res. Solid Earth 102 (B5), 10291–10298.